Science
AAAS

High-performance light-emitting diodes based on carbene-metal-amides

One Sentence Summary Spin-state inversion in rotationally-flexible linear carbene complexes enables high-performance solution-processed OLEDs.

Authors: Dawei Di[1*], Alexander S. Romanov[2*], Le Yang[1*], Johannes M. Richter[1], Jasmine P. H. Rivett[1], Saul Jones[1], Tudor H. Thomas[1], Mojtaba Abdi Jalebi[1], Richard H. Friend[1], Mikko Linnolahti[3†], Manfred Bochmann[2†] & Dan Credgington[1†]

Affiliations:

[1] Cavendish Laboratory, University of Cambridge, JJ Thomson Avenue, Cambridge, CB3 0HE, United Kingdom

[2] School of Chemistry, University of East Anglia, Earlham Road, Norwich, NR4 7TJ, United Kingdom

[3] Department of Chemistry, University of Eastern Finland, Joensuu Campus, FI-80101 Joensuu, Finland

[†]Correspondence to: djnc3@cam.ac.uk, m.bochmann@uea.ac.uk, or mikko.linnolahti@uef.fi.

[*] These authors contributed equally to this work.

Abstract:

Organic LEDs promise highly efficient lighting and display technologies. We introduce a new class of linear donor-bridge-acceptor light-emitting molecules, which enable solution-processed LEDs with near-100% internal quantum efficiency at high brightness. Key to this performance is their rapid and efficient utilization of triplet states. Using time-resolved spectroscopy, we establish that luminescence via triplets occurs within 350 ns at ambient temperature, after reverse intersystem crossing to singlets. We find that molecular geometries exist at which the singlet-triplet energy gap (exchange energy) is close to zero, such that rapid interconversion is possible. Calculations indicate that exchange energy is tuned by relative rotation of donor and acceptor moieties about the bridge. Unlike other low exchange energy systems, substantial oscillator strength is sustained at the singlet-triplet degeneracy point.

Main Text: Since the demonstration of thin-film OLEDs in the 1980s (*1*, *2*), these devices have evolved from lab curiosity to global industry. The efficiency of an OLED is fundamentally governed by the spin of bound electron-hole pairs (excitons) which form through the recombination of injected electrons and holes. The ratio of emissive singlets to dark triplets formed from randomly spin-polarized electron and hole currents is 1:3, setting a limit of 25% internal quantum efficiency (IQE) for fluorescent OLEDs. The exchange energy (singlet-triplet energy gap) is generally large and positive, around 0.5 eV. Therefore, triplets cannot usually undergo intersystem crossing (ISC) to emissive singlets. Phosphorescent OLEDs, which utilize the heavy-atom effect in platinum or iridium compounds to render triplets emissive (*3*, *4*), and thermally activated delayed

fluorescence (TADF) OLEDs, based on thermally-promoted triplet-to-singlet up-conversion for systems with low exchange energies (*5*), enable higher efficiencies. Here we show sub-microsecond luminescent harvesting of triplets in a new family of linear copper and gold carbene-metal-amides (CMAs). Importantly, this requires rapid ISC from the triplet state, which is enabled in this family of compounds at molecular configurations where the exchange energy is near zero, resulting in extremely efficient electroluminescence (EL).

We have recently shown that two-coordinate complexes of copper and gold based on cyclic (alkyl)(amino)-carbene ligands (CAACs) (*6*) can exhibit extremely high solid-state photoluminescence quantum efficiencies due to the lack of strong intermolecular interactions (*7*). To explore their use in OLEDs, we designed and synthesized CMA compounds (CAAC)AuCz (CMA1), (CAAC)CuCz (CMA2), (CAAC)AuNPh$_2$ (CMA3), and (CAAC)AuDTBCz (CMA4) (Fig. 1A) (Cz = carbazole anion, DTBCz = 3,6-di-tert-butylcarbazole anion). They are soluble in a range of organic solvents, do not undergo ligand rearrangement, and are thermally-stable to >270 °C (Table S1) (*8*). Their stability and solubility render them well-suited for solution processing, while their high decomposition temperatures allow the possibility of vacuum sublimation. Table S2 (*8*) presents their redox potentials. Absorption spectra show a molecular charge-transfer band, with an increase in extinction coefficient from ~5×10^3 M^{-1} cm^{-1} at 400 nm to >2×10^4 M^{-1} cm^{-1} for the higher-lying localized absorption bands (Figs. 1B & S1) (*8*).

To use this new class of emitter in OLEDs, we developed a multi-layer device structure with all organic layers solution-processed. A ~180 nm polymeric hole-transport/electron-blocking layer, poly(9,9-dioctylfluorene-co-N-(4-

butylphenyl)diphenylamine) (TFB), was deposited on PEDOT:PSS from toluene solution without additional crosslinking (*9*), a ~20 nm emissive layer comprising CMA1-4 dispersed as a guest emitter in a poly(9-vinylcarbazone) (PVK) host (*4, 10*) was deposited from dimethylformamide solution, while a ~70 nm layer of bathophenanthroline (BPhen) electron-transport/hole-blocking layer was deposited from methanol solution. From thickness profilometry, we found that sequential deposition of these solution-processed layers did not cause measurable thickness reduction of any of the underlying layers, suggesting minimum intermixing of the multilayer interfaces. The device energetic structure is shown in Fig. 1C.

Fig. 1D presents the maximum-EQE histogram of 182 OLEDs using CMA4. EL spectra and external quantum efficiencies (EQEs) of the best OLEDs are shown in Fig. 1E and Table 1 (additional data in Figs. S2A & S2B) (*8*). Angle-resolved EL profiles showed Lambertian emission (Fig. S2C), as is typical for OLEDs without microcavity outcoupling (*11*), allowing accurate estimation of EQE from on-axis irradiance. Commission International de l'éclairage (CIE) color coordinates showed no variation with EQE (Figs. S2D & S2E). The EQEs of the best devices at practical luminance (100 & 1000 cd m^{-2}) are >25%. While the precise structural control offered by vacuum-sublimation usually enables superior performance, the metrics of our solution-processed devices are comparable to, or exceed, those of state-of-the-art OLEDs (*5,12*) and quantum-dot LEDs (*13*). At brightness suitable for display applications, we achieve the highest quantum efficiencies reported for any solution-processed LEDs without enhanced optical outcoupling (*13, 14*). Assuming outcoupling efficiencies of 20-30% for planar

OLEDs (*5, 11, 13*), we infer a close-to-unity (80-100%) IQE for the best devices (using CMA1&4).

Time-resolved EL measurements show that emission occurs entirely via a sub-μs delayed-emission channel (Figs. 1B&1F) and there is no prompt (ns) component which would usually distinguish between geminate singlets and triplets (*15, 16*). These imply that all excitons, regardless of initial spin, contribute to luminescence. The EL lifetime decreases with increasing current density, likely due to bimolecular processes (*17*).

To understand the emission mechanism of CMAs, we measure transient photoluminescence (PL) and absorption (TA) spectra of spin-cast films. All compounds show a <1 ns prompt-PL component, and a delayed component whose lifetime is strongly temperature-dependent (Fig. 2A). Time-resolved PL spectra of CMA1 on ns-μs timescales at 300K (Fig. 2B) show a red-shift of the PL peak between prompt and delayed emission from ~490 nm at 0-2 ns, to ~540 nm at later times. The prompt emissive species is therefore spectrally distinct from the delayed emissive species. At 300K, the delayed emission accounts for >99% of the PL, and is reversibly quenched by oxygen (Fig. S3) *(8)*.

Fig. 2C presents ultrafast (fs-ps) PL (*18*) of CMA1 neat films at 300K. Emission is characterized by a single component with 4 ps lifetime. Its initial peak at 470 nm shifts to ~480 nm within 500 fs and then stabilizes, consistent with the 0-2 ns prompt component identified in Fig. 2B. ps-μs TA measurements (Fig. 2D) show the initial photo-induced absorption (PIA) near 680 nm, from the singlet exciton, converts to a single long-lived species on the same time-scale as the initial PL decay (Fig. 2G), which we assign to triplets. The triplet possesses two other co-varying PIA features in the near-

infrared (Fig. S4) *(8)*. Both singlet and triplet PIA spectra agree semi-quantitatively with calculated excited-state transitions (Fig. S5 and Table S6) *(8)*. The triplet PIA lifetime is ~300 ns at 300K (Fig. 2D). We infer that ISC to triplets occurs within 4 ps after photoexcitation, quenching the prompt fluorescence, such that the majority of excitations pass through the triplet manifold. Triplets thus act as the reservoir for delayed emission.

The delayed emission exhibits two distinct regimes. Below 100K, it peaks at ~510 nm with ~10 μs lifetime, independent of temperature (Figs. 2A & 2B), which we assign to phosphorescence. This phosphorescence redshifts by ~5 nm over the first 3 μs, consistent with diffusion of triplets to lower-energy sites. Above 100K, the lifetime of the delayed component decreases, dropping to ~350 ns at 300K (Fig. 2A), while the total PL intensity increases (Fig. S6A) *(8)*. The 300K delayed emission is ~150 meV lower in energy than the 4K phosphorescence. The characteristic activation energy (E_A) of the temperature-dependent emission is 45 meV for CMA1 (Fig. S6B). E_A and emission lifetimes for CMA2-4 are similar (Fig. S7) *(8)*. A physical model for E_A is outlined in Supplementary Materials (*8*). The PL spectra of the delayed emission in host-guest films are nearly identical to the steady-state EL spectra in devices (Fig. 1B). EL spectra typically correspond to the lowest-accessible excited state, where recombination preferentially occurs. We consider that at 300K, triplets formed electrically or after ISC from photogenerated singlets contribute to emission at a rate of $\sim 3 \times 10^6$ s^{-1}. This remarkably rapid utilization of triplets via the delayed-emission channel enables CMA-based OLEDs to maintain efficient operation at high brightness. Identifying its origin is therefore crucial to understanding their high performance.

To establish the nature of the low-energy delayed emission, we turn to the model system of molecular emitters in dilute solution, in which intermolecular interactions are suppressed and structural reorganization is unhindered. Ultrafast PL spectra for CMA1 in chlorobenzene solution (Fig. 2E) show that the PL peak shifts from 470 nm to 510 nm within 5 ps (Fig 2F). This spectral evolution is independent of solvent polarity (Fig. S8) *(8)*. The bulk of the steady-state emission in solution occurs via the delayed pathway, peaked at ~550 nm (Fig. 1B). In solution, we therefore observe ps geometrical relaxation of the photoexcited molecule which is coupled to the singlet energy.

Raman spectroscopy of solid CMA1 identifies a cluster of modes around 20-30 cm^{-1} with periods close to the observed relaxation time (Fig. S9) (*8*). Density functional theory (DFT) calculations identify these as relative rotation of donor and acceptor about the metal linkage. Their Raman peak intensity is 70% of the strength of the cluster of modes around 1500 cm^{-1}, which originate from C-N and C=C ring-stretches on the donor and acceptor moieties. Raman modes mediating electronic transitions that change the polarizability of the molecule, such as the $S_0 \rightarrow S_1$ transition, show enhanced activity (*23*). These include ring-stretching modes in π-delocalized systems, which couple to π bond order. The strong Raman activity we observe for low-frequency torsional modes is unusual, and indicates that these low-energy rotations couple to the energy of the excited singlet-state. By contrast, the analogous rotation of the substituted phenyl of CMA1 (48-52 cm^{-1}) has more typical, weak Raman scattering strength, owing to its weak coupling to the $S_0 \rightarrow S_1$ transition. The large shift in singlet energy observed over the first few ps in solution is therefore consistent with a rotational relaxation of the molecule about the metal-amide bond. Similar behavior accounts for dual-fluorescence in twisted-

intramolecular charge-transfer (TICT) emitters (*19, 20*), for which relaxation to a twisted geometry is sufficiently slow that luminescence from intermediate geometries can be observed. In solid films (Figs. 2C&2F) this early-time redshift is absent, consistent with large-scale reorganization, such as rotation, being suppressed in the solid state.

We consider that at temperatures above 100K, the sub-μs delayed emission in solid films is delayed fluorescence, rather than phosphorescence (which has ~10 μs lifetime below 100K), with reverse ISC and radiative recombination of singlets as the rate-limiting steps. Prompt fluorescence is outcompeted by ISC to triplets, which occurs in ~4 ps. This is consistent with the majority of both photo- and electrical-excitations passing through the triplet manifold before emission, as discussed. We note that, during geometric relaxation in solution, singlet emission with energies above, below and equal to that of the measured phosphorescence is observed, indicating that geometries exist at which singlet and triplet energies approach degeneracy.

To understand the link between molecular geometry and the energetic ordering of singlet and triplet states, the energies and optimized molecular structures of the ground (S_0), first excited singlet (S_1) and first excited triplet (T_1) states for CMA1-4 were calculated using DFT and time-dependent DFT (TD-DFT). Ground-state calculations yield close agreement with X-ray crystal structures (Fig. S10 and Table S3) (*8*). For all compounds, S_0 and the relaxed T_1 states correspond to a geometry with co-planar carbene and amide ligands (denoted by superscript *P*), while in the relaxed S_1 state the amide ligand is rotated by 90° relative to the carbene (denoted by superscript *R*) (Figs. 3A & S11A) (*8*). Both S_1 and T_1 have strong CT character, with excitation from the highest-occupied molecular orbital (HOMO), mostly localized on the amide, to the lowest-

unoccupied molecular orbital (LUMO), mostly localized on the carbene, contributing over 90% of the $S_0 \rightarrow S_1$ transition (Figs. 3B & S11B). Extended conjugation through the metal in the co-planar geometry is consistent with CT states contributing significantly to absorption (Figs. 1B and S1). T_1^P lies lower in energy than its co-planar singlet counterpart, S_1^P. However, increasing the dihedral angle allows S_1 to stabilize relative to T_1. Upon full relaxation, S_1^R is lower in energy than T_1^P, leading to a negative $S_1^R - T_1^P$ energy gap ($\Delta E_{ST} < 0$), which we term "rotationally accessed spin-state inversion" (RASI) (Fig. 3C). During relaxation from S_1^P to S_1^R, the singlet energy therefore passes through the triplet energy, in agreement with PL data. For CMA1, the calculated energy barrier for a full rotation of the metal-amide bond in the ground state is 143 meV, equivalent to the energy of a freely-rotatable C-C bond (*21*). We therefore consider relative rotation of the carbene and amide groups about the metal-amide bond to be the singlet relaxation mode identified by spectroscopy.

The stabilization of S_1 by rotation leads to a change of sign of the exchange energy at an intermediate dihedral angle θ_0. We consider that the rapid reverse ISC required to explain both the high delayed fluorescence rate and the high device IQE is achieved at molecular geometries close to θ_0 (Fig. 3C). ISC is likely enhanced by metal-assisted spin-orbit coupling. For CMA1, we estimate θ_0 to be ~45° (Fig. S12) (*8*), after empirically correcting for calculation errors. The calculated oscillator strength for $S_0 \rightarrow S_1$ falls to approximately zero at θ = 90° but at the singlet-triplet degeneracy point, is around half of the 0° value, yielding a transition with extinction coefficient $>10^3$ M^{-1} cm^{-1} (Fig. S12).

TD-DFT calculations suggest that in the CMA material family, RASI arises from a stronger electrostatic attraction between electron and hole in the rotated singlet geometry, enabled by the localization of electron density on the M-C bond. In the triplet state, the more delocalized electron density at this bond leads to a weaker attraction, insufficient to overcome the torsional potential associated with increasing the dihedral angle. Electron density maps are presented in Fig. S13 (*8*). This behavior contrasts with carbene-metal-halide (CMH) molecules involving the same carbene ligands (*7*). For CMHs, the calculated ΔE_{ST} was 300-400 meV, too large to allow reverse ISC. The behavior of the CMAs also contrasts with 3-coordinate Cu(I)-compounds where rotational freedom does not allow spin-state inversion (*22*).

Combined, these data provide a framework for understanding the luminescence behavior of CMA emitters in different material phases. Fig. 3D presents a schematic of the steady-state PL peak energies of CMA1 in phases with differing access to rotated states. The highest PL energy (2.6 eV) is observed for polycrystalline powders, where all molecules are constrained into a near-coplanar configuration (Fig. S10). Spin-cast dilute (1.5 wt%) host-guest films show 2.45 eV emission; more concentrated (20%) host-guest films emit at 2.4 eV, while neat films emit at ~2.3 eV. In the spin-cast amorphous phase, molecules deposited at room-temperature will deviate stochastically from the ground-state geometry and exist as a mixture of rotamers, consistent with photothermal deflection spectroscopy of CMA1 neat films showing a broad Urbach tail (Fig. S1). Diffusion to a range of rotated states is thus easier in spin-cast films than in crystal, and depends on the local density of emitters. Dynamic access to different molecular configurations may also be possible. In the solution phase, molecules dynamically

reorganize to the lowest-energy configuration; steady-state emission in solution is at ~2.2 eV. We therefore observe a direct correlation between the availability of rotated molecular geometries and the energy of emission, whether such geometries are accessed dynamically or via diffusion.

We have synthesized a new class of materials for high-performance OLEDs exhibiting rapid emission via the triplet state, such that all electron-hole recombination events can lead to luminescence. At 300K, the emission lifetimes for CMA1 is 350 ns, considerably faster than that achieved to date in efficient iridium-based phosphorescent emitters (*24*,*25*) (typical lifetimes >1.5 μs) and efficient TADF emitters (typical lifetimes > 5 μs) (*5, 26*). This is possible due to the existence of molecular configurations which achieve low exchange energies while still retaining appreciable oscillator strength, in contrast to TADF materials for which low exchange energy is achieved at the expense of oscillator strength (*27*). Sub-microsecond emission is particularly beneficial for efficient high-brightness OLED operation, as we demonstrate, and for avoiding degradation pathways arising from bimolecular annihilation events (*17*).

References and Notes:

1. C. Tang, S. VanSlyke, Organic electroluminescent diodes. *Appl. Phys. Lett*. **51**, 913 (1987).
2. J. Burroughes *et al*., Light-emitting diodes based on conjugated polymers, *Nature* **347**, 539-541 (1990).
3. M. Baldo *et al*., Highly efficient phosphorescent emission from organic electroluminescent devices, *Nature* **395**, 151-154 (1998).

4. Y. Ma, H. Zhang, J. Shen, C. Che, Electroluminescence from triplet metal—ligand charge-transfer excited state of transition metal complexes, *Synthetic Metals* **94**, 245-248 (1998).
5. H. Uoyama, K. Goushi, K. Shizu, H. Nomura, C. Adachi, Highly efficient organic light-emitting diodes from delayed fluorescence, *Nature* **492**, 234-238 (2012).
6. G. Frey, R. Dewhurst, S. Kousar, B. Donnadieu, G. Bertrand, Cyclic (alkyl)(amino)carbene gold(I) complexes: A synthetic and structural investigation, *J. Organomet. Chem.* **693**, 1674-1682 (2008).
7. A. Romanov *et al.*, Highly photoluminescent copper carbene complexes based on prompt rather than delayed fluorescence, *Chem. Commun.* **52**, 6379-6382 (2016).
8. Full details can be found in the supplementary materials on *Science* Online.
9. R. Png *et al.*, High-performance polymer semiconducting heterostructure devices by nitrene-mediated photocrosslinking of alkyl side chains, *Nat. Mater.* **9**, 152-158 (2009).
10. D. Abbaszadeh *et al.*, Elimination of charge carrier trapping in diluted semiconductors, *Nat. Mater.* **15**, 628-633 (2016).
11. N. Greenham, R. Friend, D. Bradley, Angular Dependence of the Emission from a Conjugated Polymer Light-Emitting Diode: Implications for efficiency calculations, *Adv. Mater.* **6**, 491-494 (1994).
12. S. Reineke *et al.*, White organic light-emitting diodes with fluorescent tube efficiency, *Nature* **459**, 234-238 (2009).
13. X. Dai *et al.*, Solution-processed, high-performance light-emitting diodes based on quantum dots, *Nature* **515**, 96-99 (2014).

14. N. Aizawa *et al*., Solution-processed multilayer small-molecule light-emitting devices with high-efficiency white-light emission, *Nat. Commun.* **5**, 5756 (2014).
15. D. Kondakov, Characterization of triplet-triplet annihilation in organic light-emitting diodes based on anthracene derivatives, *J. Appl. Phys.* **102**, 114504 (2007).
16. B. Wallikewitz, D. Kabra, S. Gélinas, R. Friend, Triplet dynamics in fluorescent polymer light-emitting diodes, *Phys. Rev. B* **85**, 045209 (2012).
17. N. Giebink, S. Forrest, Quantum efficiency roll-off at high brightness in fluorescent and phosphorescent organic light emitting diodes, *Phys. Rev. B* **77**, 235215 (2008).
18. K. Chen, J. Gallaher, A. Barker, J. Hodgkiss, Transient Grating Photoluminescence Spectroscopy: An Ultrafast Method of Gating Broadband Spectra, *J. Phys. Chem. Lett.* **5**, 1732-1737 (2014).
19. S. Sasaki, G. Drummen, G. Konishi, Recent advances in twisted intramolecular charge transfer (TICT) fluorescence and related phenomena in materials chemistry, *J. Mater. Chem. C* **4**, 2731-2743 (2016).
20. A. Siemiarczuk, Z. Grabowski, A. Krówczyński, M. Asher, M. Ottolenghi, Two emitting states of excited p-(9-anthryl)-n,n-dimethylaniline derivatives in polar solvents, *Chem. Phys. Lett.* **51**, 315-320 (1977).
21. J. Zheng, K. Kwak, J. Xie, M. Fayer, Ultrafast Carbon-Carbon Single-Bond Rotational Isomerization in Room-Temperature Solution, *Science* **313**, 1951-1955 (2006).
22. M. Leitl, V. Krylova, P. Djurovich, M. Thompson, H. Yersin, Phosphorescence versus thermally activated delayed fluorescence. Controlling singlet-triplet splitting in brightly emitting and sublimable Cu(I) compounds. *J. Am. Chem. Soc.* **45**, 16032–

16038 (2014).

23. E. Ehrenfreund, Z. Vardeny, O. Brafman, B. Horovitz, Amplitude and phase modes intrans-polyacetylene: Resonant Raman scattering and induced infrared activity, *Phys. Rev. B* **36**, 1535-1553 (1987).
24. T. Sajoto *et al*., Temperature Dependence of Blue Phosphorescent Cyclometalated Ir(III) Complexes, *J. Am. Chem. Soc.* **131**, 9813-9822 (2009).
25. M. Baldo, S. Lamansky, P. Burrows, M. Thompson, S. Forrest, Very high-efficiency green organic light-emitting devices based on electrophosphorescence, *Appl. Phys. Lett.* **75**, 4 (1999).
26. Y. Tao *et al*., Thermally Activated Delayed Fluorescence Materials Towards the Breakthrough of Organoelectronics, *Adv. Mater.* **26**, 7931-7958 (2014).
27. R. Gómez-Bombarelli *et al*., Design of efficient molecular organic light-emitting diodes by a high-throughput virtual screening and experimental approach, *Nat. Mater.* **15**, 1120-1127 (2016).
28. A. Romanov, M. Bochmann, Gold(I) and Gold(III) Complexes of Cyclic (Alkyl)(amino)carbenes, *Organometallics* **34**, 2439-2454 (2015).
29. G. Gritzner, J. Kůta, Recommendations on reporting electrode potentials in nonaqueous solvents, *Electrochim. Acta* **29**, 869-873 (1984).
30. *Programs CrysAlisPro*, Oxford Diffraction Ltd., Abingdon, UK (2010).
31. G. Sheldrick, A short history of SHELX, *Acta Cryst Sect A* **64**, 112-122 (2007).
32. F. Furche, D. Rappoport, Density functional methods for excited states: equilibrium structure and electronic spectra in *Computational Photochemistry* (ed. M. Olivuccim) 93-128 (Elsevier, Amsterdam, 2005).

33. J. Perdew, K. Burke, M. Ernzerhof, Generalized Gradient Approximation Made Simple, *Phys. Rev. Lett.* **77**, 3865-3868 (1996).

34. C. AdamoV. Barone, Toward reliable density functional methods without adjustable parameters: The PBE0 model, *J. Chem. Phys.* **110**, 6158 (1999).

35. F. Weigend, M. Häser, H. Patzelt, R. Ahlrichs, RI-MP2: optimized auxiliary basis sets and demonstration of efficiency, *Chem. Phys. Lett.* **294**, 143-152 (1998).

36. F. Weigend, R. Ahlrichs, Balanced basis sets of split valence, triple zeta valence and quadruple zeta valence quality for H to Rn: Design and assessment of accuracy, *Phys. Chem. Chem. Phys.* **7**, 3297 (2005).

37. K. Peterson, D. Figgen, E. Goll, H. Stoll, M. Dolg, Systematically convergent basis sets with relativistic pseudopotentials. II. Small-core pseudopotentials and correlation consistent basis sets for the post-d group 16–18 elements, *J. Chem. Phys.* **119**, 11113 (2003).

38. D. Andrae, U. Haeussermann, M. Dolg, H. Stoll, H. Preuss, Energy-adjustedab initio pseudopotentials for the second and third row transition elements, *Theor. Chim. Acta* **77**, 123-141 (1990).

39. M. Bühl, C. Reimann, D. Pantazis, T. Bredow, F. Neese, Geometries of Third-Row Transition-Metal Complexes from Density-Functional Theory, *J. Chem. Theory Comput.* **4**, 1449-1459 (2008).

40. R. Kang, H. Chen, S. Shaik, J. Yao, Assessment of Theoretical Methods for Complexes of Gold(I) and Gold(III) with Unsaturated Aliphatic Hydrocarbon: Which Density Functional Should We Choose?, *J. Chem. Theory Comput.* **7**, 4002-4011 (2011).

41. C. Adamo, G. Scuseria, V. Barone, Accurate excitation energies from time-dependent density functional theory: Assessing the PBE0 model, *J. Chem. Phys.* **111**, 2889 (1999).
42. C. Adamo, V. Barone, R. Subra, The mechanism of spin polarization in aromatic free radicals, *Theoretical Chemistry Accounts: Theory, Computation, and Modeling (Theor. Chim. Acta)* **104**, 207-209 (2000).
43. D. Jacquemin, A. Planchat, C. Adamo, B. Mennucci, TD-DFT Assessment of Functionals for Optical 0–0 Transitions in Solvated Dyes, *J. Chem. Theory Comput.* **8**, 2359-2372 (2012).
44. A. Laurent, M. Medved, D. Jacquemin, Using TD-DFT to probe the nature of donor-acceptor Stenhouse adduct (DASA) photochromes, *ChemPhysChem* , DOI: 10.1002/cphc.201600041 (2016).
45. I. Koshevoy *et al.*, Intensely Luminescent Alkynyl−Phosphine Gold(I)−Copper(I) Complexes: Synthesis, Characterization, Photophysical, and Computational Studies, *Inorg. Chem.* **48**, 2094-2102 (2009).
46. I. Koshevoy *et al.*, Luminescent Gold(I) Alkynyl Clusters Stabilized by Flexible Diphosphine Ligands, *Organometallics* **33**, 2363-2371 (2014).
47. Y. Zhao, D. Truhlar, The M06 suite of density functionals for main group thermochemistry, thermochemical kinetics, noncovalent interactions, excited states, and transition elements: two new functionals and systematic testing of four M06 functionals and 12 other functionals, *Theor Chem Account* **119**, 525-525 (2008).

48. TURBOMOLE V6.3 2011, a development of University of Karlsruhe and Forschungszentrum Karlsruhe GmbH, 1989 –2007, TURBOMOLE GmbH, since 2007; available from http://www.turbomole.com.
49. M. Frisch *et al*., Gaussian 09, Revision C.01, Gaussian, Inc., Wallingford, CT (2010).

Acknowledgments: We thank Dr. M. Roberts and Cambridge Display Technology Ltd. (Company No. 02672530) for re-calibration of OLED measurements and for angular emission tests. We thank Dr. A. Morris, Dr. H. Stern, Dr. A. Sadhanala, B. Zhu, L. Meraldi, J. Ratanapreechachai and J. Nisbett for help and discussions. D.D. and R.H.F. acknowledge the Department of Physics (Cambridge) and the KACST–Cambridge University Joint Centre of Excellence for support. L.Y. thanks the Singapore Agency for Science, Technology and Research (A*STAR) for a PhD studentship. J. M. R. acknowledges Winton Program for the Physics of Sustainability for support. J. P. H. R. acknowledges the Cambridge NanoDTC (EP/L015978/1). M.L. acknowledges support by the Academy of Finland (Project 251448). The computations were made possible by use of the Finnish Grid Infrastructure and Cloud Infrastructure. This work was supported by Engineering and Physical Sciences Research Council (EPSRC) (Grant No. EP/M005143/1) and the European Research Council (ERC). M.B. is an ERC Advanced Investigator Award holder (Grant No. 338944-GOCAT). D.C. and S.J. acknowledge the Royal Society for support. A patent applications has been filed covering the CMA materials described herein. Patent application: PCT/GB2016/052797. Inventors: M. Bochmann, A. S. Romanov, D. Credgington, D. Di, L. Yang. A collaboration agreement exists between Cambridge and UEA which includes restrictions on the transfer of materials. CCDC-1472605 (CMA1), CCDC-1472607 (CMA2), CCDC-1472606 (CMA3) and CCDC-1473622 (CMA4) contain supplementary crystallographic data, which can be obtained free of charge from the Cambridge Crystallographic Data Centre via www.ccdc.cam.ac.uk/data_request/cif.

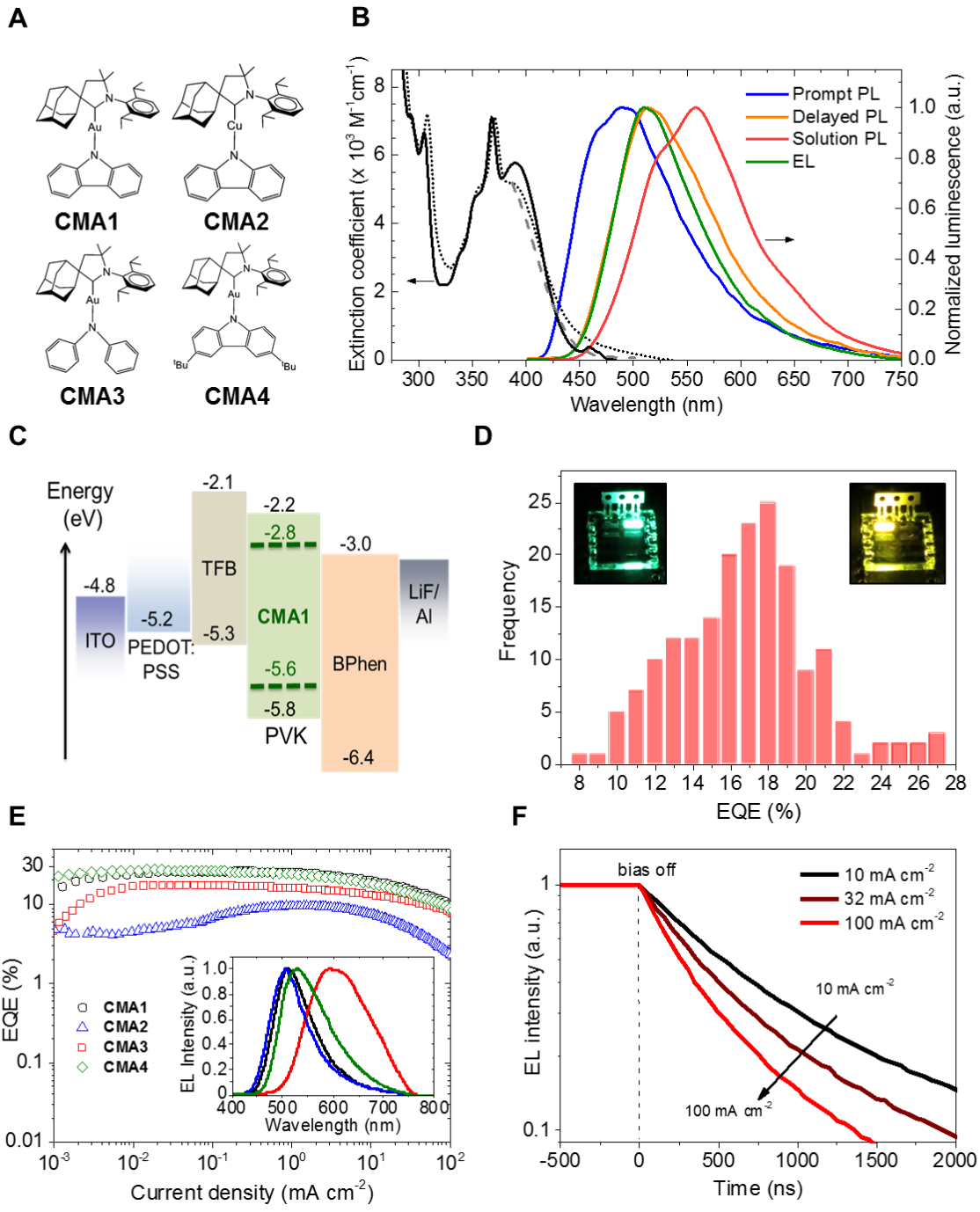

Fig. 1 Chemical structures, absorption/emission spectra and OLED performance.

(A) Chemical structures of CMAs. **(B)** (Left axis) Molar extinction coefficients of CMA1 in THF solution (solid) and absorption in neat film (dot). Overlaid photothermal deflection spectrum (dash) indicates the film absorption tail arises primarily from

scattering. To convert from molar extinction ($M^{-1}\,cm^{-1}$) to film absorption (cm^{-1}), multiply by 2. (Right axis) PL and EL spectra of spin-cast films of CMA1 dispersed in PVK host (at 20 wt%), and in solution **(C)** Energy level diagram of a CMA1 device. **(D)** Peak-EQE Histogram of 182 CMA4 devices (Most typical = ~18%; highest = 27.5%). Insets: photographs of CMA1 (left) and CMA3 (right) devices. Device area = 5.25 mm^2. **(E)** EQE curves and EL spectra (inset) for devices utilizing CMA1-4 dispersed at 20 wt% in PVK. **(F)** Transient-EL curves measured after holding a CMA1 device at various steady-state current densities.

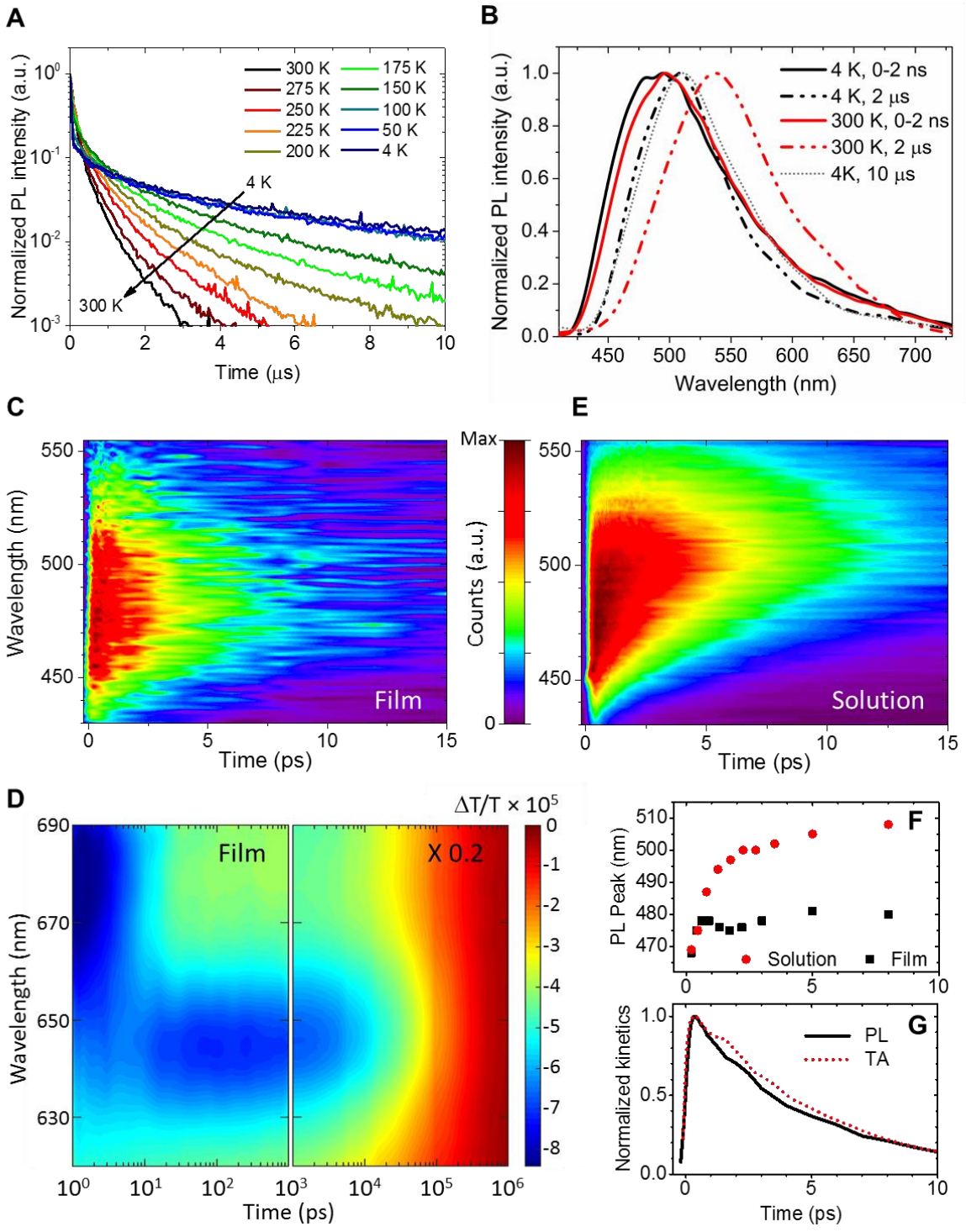

Fig. 2 Transient photophysical characterization of CMA1. (**A**) Temperature-dependent ns-μs PL kinetics measured using an electrically gated ICCD. **(B)** Prompt (t < 2 ns) and delayed (t = 2 μs) PL spectra at 300K. The 10-μs spectrum at 4K highlights the

slight evolution of the phosphorescence spectrum. **(C)** Ultrafast Kerr-gated PL measurement of CMA1 neat film (300K), color scale indicates total counts above background. (**D**) TA spectra of CMA1 neat film (300K) on ps-μs timescales. The initial excited state absorption associated with the singlet is at 680 nm. The narrower blue-shifted band centered at 645 nm is associated with the triplet. **(E)** Ultrafast PL measurement of CMA1 (0.1 wt%) in chlorobenzene (300K). **(F)** Evolution of PL peak position for the first 10 ps of the ultrafast-PL decays. The solution sample exhibits a substantial red shift on this time-scale, which is absent in the solid film. **(G)** Decay kinetics of spectrally-integrated PL intensity and the 680 nm PIA in neat CMA1 films. Both share a common 4-ps decay time and the triplet PIA at 645 nm grows with the same timescale. All samples pumped at 400 nm.

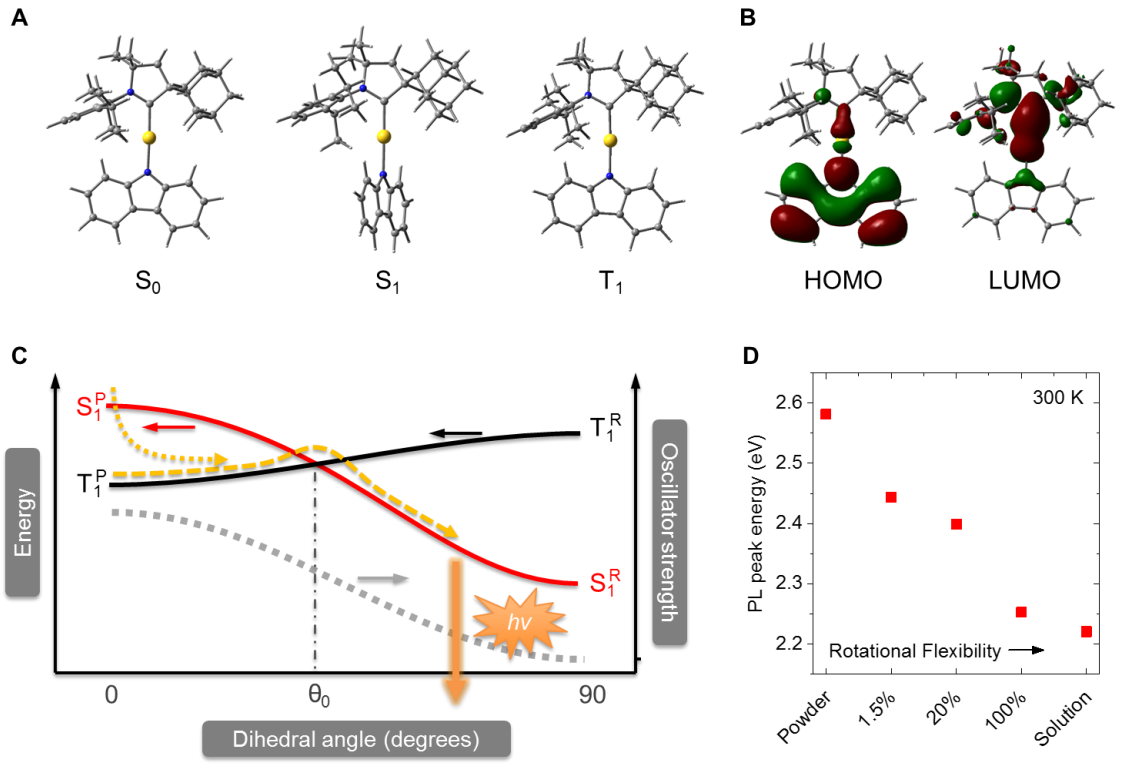

Fig. 3 DFT calculations and the RASI mechanism. **(A)** Optimized geometries of CMA1 in S_0, S_1 and T_1 states. **(B)** HOMO and LUMO wavefunctions of CMA1 from DFT and TD-DFT calculations, isovalue = 0.02 (electrons/bohr^3)$^{1/2}$. **(C)** Schematic of the RASI mechanism based on TD-DFT calculations, illustrating the stabilization of S_1 and destabilization of T_1 as the dihedral angle between donor and acceptor increases from co-planar (P) to rotated (R) geometries. Oscillator strength for the S_1 to the ground state varies approximately sinusoidally with dihedral angle. S_1-T_1 degeneracy occurs at angle θ_0. Trajectories for photogenerated singlets (dot) and electrically-generated triplets (dash) are indicated. **(D)** Steady-state PL peak energies of CMA1 in (from left to right) polycrystalline powder, 1.5 wt% in PVK, 20 wt% in PVK, neat film (100 wt%) and 0.1 wt% in chlorobenzene.

Table 1: Summary of OLED performances (best devices). Efficiencies at different brightness (100 cd m^{-2} and 1000 cd m^{-2}) are shown.

Emitter	Turn-on Voltage (V)	EQE (%)	Current Efficiency (cd A^{-1})	Power Efficiency (lm W^{-1})	Max. Luminance (cd m^{-2})
		Max/100/1000 cd m^{-2}	Max/100/1000 cd m^{-2}	Max/100/1000 cd m^{-2}	
CMA1	2.6	26.3/ 26.1/ 25.2	76.3/ 75.8/ 73.0	62.7/ 50.0/ 37.0	44700
CMA2	3.4	9.7/ 8.9/ 9.2	30.4 /28.0/ 29.0	11.8/ 11.7/ 9.3	7790
CMA3	3.0	17.9/ 17.3/ 15.5	45.2/ 43.7/ 39.1	33.6/ 25.0/ 17.0	39540
CMA4	2.6	27.5/ 26.6/ 24.5	87.1/ 84.5/ 77.9	75.1/ 50.2/ 35.5	73100

Supplementary Materials:

Supplementary Materials for

High-performance light-emitting diodes based on carbene-metal-amides

Dawei Di[1*], Alexander S. Romanov[2*], Le Yang[1*], Johannes M. Richter[1], Jasmine P. H. Rivett[1], Saul Jones[1], Tudor H. Thomas[1], Mojtaba Abdi Jalebi[1], Richard H. Friend[1], Mikko Linnolahti[3†], Manfred Bochmann[2†] & Dan Credgington[1†]

[1] Cavendish Laboratory, University of Cambridge, JJ Thomson Avenue, Cambridge, CB3 0HE, United Kingdom.
[2] School of Chemistry, University of East Anglia, Earlham Road, Norwich, NR4 7TJ, United Kingdom
[3] Department of Chemistry, University of Eastern Finland, Joensuu Campus, FI-80101 Joensuu, Finland

[†] Correspondence to: djnc3@cam.ac.uk, m.bochmann@uea.ac.uk, or mikko.linnolahti@uef.fi.

[*] These authors contributed equally to this work.

This PDF file includes:

Materials and Methods

Synthesis of carbene metal amides

General Considerations. Unless stated otherwise all reactions were carried out in air. Solvents were distilled and dried as required. Sodium tert-butoxide, $HNPh_2$, carbazole and 3,6-di-tBucarbazole were purchased from Sigma-Aldrich and used as received. Complexes (CAAC)MCl (M = Cu and Au) were obtained as described (*28*). Spectra of ^1H, $^{13}C\{^1H\}$ were recorded using a Bruker Avance DPX-300 MHz NMR spectrometer. ^1H NMR (300.13 MHz) and $^{13}C\{1H\}$ (75.47 MHz) were referenced to CD_2Cl_2 at δ 5.32 (^{13}C, δ 53.84). All electrochemical experiments were performed using an Autolab PGSTAT 302N computer-controlled potentiostat. Cyclic voltammetry (Fig. S14) was performed using a three-electrode configuration consisting of either a glassy carbon macrodisk working electrode (GCE) (diameter of 3 mm; BASi, Indiana, USA) combined with a Pt wire counter electrode (99.99%; GoodFellow, Cambridge, UK) and an Ag wire pseudoreference electrode (99.99%; GoodFellow, Cambridge, UK). The GCE was polished between experiments using alumina slurry (0.3 μm), rinsed in distilled water and subjected to brief ultrasonication to remove any adhered alumina microparticles. The metal electrodes were then dried in an oven at 100°C to remove any residual traces of water, the GCE was left to air dry and residual traces of water were removed under vacuum. The Ag wire pseudoreference electrodes were calibrated to the ferrocene/ferrocenium couple in MeCN at the end of each run to allow for any drift in potential, following IUPAC recommendations (*29*). All electrochemical measurements were performed at ambient temperatures under an inert Ar atmosphere in MeCN containing complex under study (1.4 mM) and supporting electrolyte [n-Bu_4N][PF_6] (0.13 M). Data were recorded with Autolab NOVA software (v. 1.11). Elemental analyses were performed by the London Metropolitan University.

Synthesis of (CAAC)AuCz (CMA1). A mixture of (CAAC)AuCl (0.2 g, 0.33 mmol), NaO^{t}Bu (33 mg, 0.34 mmol) and carbazole (57 mg, 0.33 mmol) in dry THF (20 mL) under an argon atmosphere was stirred for 6 h. The mixture was centrifuged and solution of the product was decanted. All volatiles were evaporated in vacuum to give an off-white powder. Yield: 0.23 g (0.31 mmol, 94 %). Product usually contains THF as a solvate and therefor was kept under vacuum for 2 h at 80 °C to remove solvate molecules.

^1H NMR (300 MHz, CD_2Cl_2): δ 7.92 (d, *J* = 7.8 Hz, 2H, carbazole CH^4), 7.69 (t, *J* = 7.8 Hz, 1H, aryl), 7.46 (d, *J* = 7.8 Hz, 2H, aryl), 7.08 (t, *J* = 7.8 Hz, 2H, carbazole CH^2), 6.90 (t, *J* = 7.8 Hz, 2H, carbazole CH^3), 6.65 (d, *J* = 7.8 Hz, 2H, carbazole CH^1), 4.34 (d, *J* = 13.5 Hz, 2H, CH_2), 2.92 (sept, *J* = 6.6 Hz, 2H, C*H*Me_2), 2.44–1.82 (m, 14H, adamantyl CH and CH_2), 1.44 (s, 6H, C($C\underline{H}_3$)), 1.34 (d, *J* = 6.6 Hz, 12H, CH*Me*$_2$). ^{13}C NMR (75 MHz, CD_2Cl_2) δ 244.6 (C carbene), 150.0 (*ipso*-CN carbazole), 146.2 (*o*-C), 136.7 (*ipso*-C), 129.9 (*p*-CH), 125.7 (*m*-CH), 124.4 (*ipso*-C carbazole), 123.7 (carbazole CH^2), 119.4 (carbazole CH^4), 116.2 (carbazole CH^3), 114.2 (carbazole CH^1), 77.4 (C_q), 64.5 (C_q), 49.2 (CH_2), 39.4 (CH_2), 37.7 (CH), 35.8 (CH_2), 34.8 (CH_2), 29.5, 28.6, 27.8, 26.5, 23.4 (CH_3). Anal. Calcd. for $C_{39}H_{47}N_2Au$ (740.76): C, 63.23; H, 6.39; N, 3.78. Found: C, 63.34; H, 6.43; N, 3.71.

Synthesis of (CAAC)CuCz (CMA2). Following the procedure described for CMA1, the complex was made from (CAAC)CuCl (0.2 g, 0.42 mmol), NaO^{t}Bu (44 mg, 0.42 mmol) and carbazole (70 mg, 0.42 mmol) as a yellow powder. Yield: 0.22 g (0.36 mmol, 86%).

^{1}H NMR (300 MHz, CD_2Cl_2): δ 7.90 (d, *J* = 7.4 Hz, 2H, carbazole CH^4), 7.72 (t, *J* = 7.8 Hz, 1H, aromatic CH), 7.49 (d, *J* = 7.8 Hz, 2H, aryl), 7.04 (t, *J* = 7.4 Hz, 2H, carbazole CH^2), 6.89 (t, *J* = 7.4 Hz, 2H, carbazole CH^3), 6.33 (d, *J* = 7.4 Hz, 2H, carbazole CH^1), 3.89 (d, *J* = 12.3 Hz, 2H, CH_2), 2.97 (sept, *J* = 6.6 Hz, 2H, C*H*Me$_2$), 2.33–1.88 (m, 14H, adamantyl CH and CH_2), 1.42 (s, 6H, CMe$_2$), 1.35 (d, *J* = 6.6 Hz, 6H, CH*Me*$_2$), 1.18 (d, *J* = 6.6 Hz, 6H, CH*Me*$_2$). ^{13}C NMR (75 MHz, CD_2Cl_2) δ 254.1 (C carbene), 150.3 (*ipso*-CN carbazole), 146.1 (*o*-C), 136.4 (*ipso*-C), 129.9 (*p*-CH), 125.6 (*m*-CH), 124.4 (*ipso*-C carbazole), 123.4 (carbazole CH^2), 119.2 (carbazole CH^4), 115.5 (carbazole CH^3), 114.8 (carbazole CH^1), 79.1 (C_q), 65.4 (C_q), 48.4 (CH_2), 38.9 (CH_2), 37.7 (CH), 36.5 (CH_2), 34.5 (CH_2), 29.64, 29.62, 28.7, 27.5, 26.5, 22.7 (CH_3). Anal. Calcd. for $C_{39}H_{47}N_2Cu$ (607.35): C, 77.13; H, 7.80; N, 4.61. Found: C, 77.07; H, 7.89; N, 4.70.

Synthesis of (CAAC)AuNPh$_2$ (CMA3). Following the procedure described for CMA1, the complex was made from (CAAC)AuCl (0.2 g, 0.33 mmol), NaOtBu (33 mg, 0.33 mmol) and diphenylamine (56 mg, 0.33 mmol) as a yellow powder. Yield: 0.24 g (0.32 mmol, 98%).

^{1}H NMR (300 MHz, CD_2Cl_2): δ 7.58 (t, *J* = 7.8 Hz, 1H, aryl), 7.34 (d, *J* = 7.8 Hz, 2H, aryl), 6.87 (t, *J* = 7.2 Hz, 4H, *m*-CH aniline), 6.60 (d, *J* = 7.2 Hz, 4H, *o*-CH aniline), 6.46 (t, *J* = 8.1 Hz, 2H, *p*-CH aniline), 4.05 (d, *J* = 13.8 Hz, 2H, CH_2), 2.81 (sept, *J* = 6.6 Hz, 2H, C*H*Me$_2$), 2.35–1.74 (m, 14H, adamantyl CH and CH_2), 1.36 (s, 6H CMe$_2$), 1.31 (d, *J* = 6.6 Hz, 6H, CH*Me*$_2$), 1.30 (d, *J* = 6.6 Hz, 6H, CH*Me*$_2$). ^{13}C NMR (75 MHz, CD_2Cl_2) δ 242.6 (carbene C), 155.5 (*i*-C$_{amide}$), 145.7 (*o*-C), 136.5 (*i*-C), 129.7 (*p*-CH), 128.6 (*m*-C$_{amide}$), 125.5 (*m*-CH), 120.9 (*o*-C$_{amide}$), 116.9 (*p*-C$_{amide}$), 76.8 (C_q), 64.3 (C_q), 49.2 (CH_2), 39.4 (CH_2), 37.4 (CH), 35.2 (CH_2), 34.8 (CH_2), 29.4, 28.3, 27.7, 26.2, 23.4 (CH_3). Anal. Calcd. for $C_{39}H_{49}N_2Au$ (742.78) C, 63.06; H, 6.65; N, 3.77. Found: C, 63.19; H, 6.71; N, 3.72.

Synthesis of (CAAC)AuDTBCz (CMA4). Following the procedure described for CMA1, the complex was made from (CAAC)AuCl (0.2 g, 0.33 mmol), NaOtBu (33 mg, 0.34 mmol) and 3,6-di-tBucarbazole (92 mg, 0.33 mmol) as a yellow powder. Yield: 0.255 g (0.33 mmol, 91%).

^{1}H NMR (300 MHz, CD_2Cl_2): δ 7.93 (d, *J* = 2.1 Hz, 2H, carbazole CH^4), 7.69 (t, *J* = 8.0 Hz, 1H, aromatic CH), 7.46 (d, *J* = 8.0 Hz, 2H, aryl), 7.15 (dd, *J* = 8.8 and 2.1 Hz, 2H, carbazole CH^2), 6.58 (d, *J* = 8.8 Hz, 2H, carbazole CH^1), 4.34 (d, *J* = 11.8 Hz, 2H, CH_2), 2.90 (sept, *J* = 7.2 Hz, 2H, C*H*Me$_2$), 2.34–1.87 (m, 14H, adamantyl CH and CH_2), 1.42 (s, 6H, CMe$_2$), 1.39 (s, 18H, ^{t}Bu), 1.35 (d, *J* = 7.2 Hz, 6H, CH*Me*$_2$) overlapping with 1.34 (d, *J* = 7.2 Hz, 6H, CH*Me*$_2$). ^{13}C NMR (75 MHz, CD_2Cl_2) δ 244.6 (C carbene), 148.4 (*ipso*-CN carbazole), 146.1 (*o*-C), 146.0 (*ipso*-C), 138.7 (*ipso*-C^3 carbazole ^{t}Bu), 136.6 (*ipso*-C), 129.8 (*p*-CH), 125.5 (*m*-CH), 124.0 (*ipso*-C carbazole), 121.4 (carbazole CH^2), 115.3 (carbazole CH^4), 113.3 (carbazole CH^1), 77.2 (C_q), 64.4 (C_q), 49.1 (CH_2),

39.3 (CH_2), 37.5 (CH), 35.7 (CH_2), 34.7 (C, ^{t}Bu), 34.6 (CH_2), 29.49, 28.5, 27.7, 26.4, 23.3 (CH_3). Anal. Calcd. for $C_{47}H_{63}N_2Au$ (852.98): C, 66.18; H, 7.44; N, 3.28. Found: C, 66.27; H, 7.56; N, 3.22.

For crystallographic and electrochemical characterization of CMA compounds see Figs. S10 & S14, and Table S2.

X-Ray crystallography

The crystals suitable for X-ray study for CMA2 and CMA4 were obtained by layering CH_2Cl_2 solution with hexanes at -20 °C. Gold complexes (CMA1 and CMA3) were crystallized by slow evaporation of benzene solution. Crystals were mounted in oil on glass fibres and fixed in the cold nitrogen stream on a diffractometer. X-ray diffraction experiment was carried out with an Oxford Diffraction Xcalibur-3/Sapphire3-CCD diffractometer, using graphite monochromated Mo K_α radiation (λ = 0.71073 Å) at 140 K. Data were processed using the CrystAlisPro-CCD and -RED software (*30*).

The principal crystallographic data **CMA1**: $C_{39}H_{47}AuN_2$, orthorhombic, space group $P2_12_12_1$, a = 9.4256(1) Å, b = 15.6507(2) Å, c = 21.8140(2) Å, V = 3217.94(6) Å^3, Z = 4, d_{calc} = 1.529 g cm^{-3}, μ = 4.601 mm^{-1}, yellow/prism, crystal size 0.45 × 0.42 × 0.31 mm, F(000) = 1496, T_{min}/T_{max} 0.3296/0.2313, R_1 = 0.0156 (from 6203 unique reflections with $I>2\sigma(I)$) and wR_2 = 0.0379 (from all 6307 unique reflections), GOF = 1.046, $\Delta\rho_{min}/\Delta\rho_{max}$ = 0.706/–0.310. **CMA2**: $C_{39}H_{47}AuN_2\cdot CH_2Cl_2$, monoclinic, space group $P2_1/n$, a = 10.8520(2) Å, b = 18.8311(3) Å, c = 18.3279(4) Å, β = 106.337(2)°, V = 3594.17(12) Å^3, Z = 4, d_{calc} = 1.279 g cm^{-3}, μ = 0.786 mm^{-1}, colourless/prism, crystal size 0.49 × 0.41 × 0.23 mm, F(000) = 1464, T_{min}/T_{max} 0.8398/0.6993, R_1 = 0.0361 (from 7150 unique reflections with $I>2\sigma(I)$) and wR_2 = 0.0989 (from all 8668 unique reflections), GOF = 1.063, $\Delta\rho_{min}/\Delta\rho_{max}$ = 0.738/–0.697. **CMA3**: $C_{39}H_{49}AuN_2\cdot C_6H_6$, monoclinic, space group $P2_1/c$, a = 12.3977(2), b = 20.1046(3) Å, c = 15.7158(2) Å, β = 107.794(2)°, V = 3729.78(9) Å^3, Z = 4, d_{calc} = 1.462 g cm^{-3}, μ = 3.978 mm^{-1}, yellow/plate, crystal size 0.26 × 0.23 × 0.15 mm, F(000) = 1672, T_{min}/T_{max} 0.5868/0.4244, R_1 = 0.0226 (from 7931 unique reflections with $I>2\sigma(I)$) and wR_2 = 0.0529 (from all 9002 unique reflections), GOF = 1.045, $\Delta\rho_{min}/\Delta\rho_{max}$ = 1.357/–0.998. **CMA4**: $C_{47}H_{63}AuN_2\cdot 2CH_2Cl_2$, monoclinic, space group $P2_1/c$, a = 12.7613(4) Å, b = 15.3884(3) Å, c = 24.1466(5) Å, β = 95.427(2)°, V = 4720.6(2) Å^3, Z = 4, d_{calc} = 1.439 g cm^{-3}, μ = 3.377 mm^{-1}, colourless/plate, crystal size 0.26 × 0.17 × 0.09 mm, F(000) = 2088, T_{min}/T_{max} 0.7509/0.4738, R_1 = 0.0360 (from 11579 unique reflections with $I>2\sigma(I)$) and wR_2 = 0.0798 (from all 14388 unique reflections), GOF = 1.077, $\Delta\rho_{min}/\Delta\rho_{max}$ = 1.836/–1.205. Alert B is originated from the restriction of the resolution range of the data which was imposed by SHEL statement on the final refinement step. One of the ^{t}Bu-groups was disordered into two positions with equal occupancies for CMA4. DFIX statement was used to adopt a tetrahedral geometry for the disordered groups of atoms. The structures were solved by direct methods and refined by the full-matrix least-squares against F^2 in an anisotropic (for non-hydrogen atoms) approximation. All hydrogen atom positions were refined in isotropic approximation in "riding" model with the $U_{iso}(H)$ parameters equal to 1.2 $U_{eq}(C_i)$, for methyl groups equal to 1.5 $U_{eq}(C_{ii})$, where $U(C_i)$ and $U(C_{ii})$ are respectively the equivalent thermal parameters of the carbon atoms to which

the corresponding H atoms are bonded. All calculations were performed using the SHELXTL software (*31*).

DFT and time-dependent DFT computations

The ground states and excited states were optimized by the density functional theory (DFT) (*32*) and time-dependent density functional theory (TD-DFT) using the hybrid density functional PBE0 method (*33, 34*) in combination with def2-TZVP basis set of Ahlrichs and coworkers (*35, 36*). Relativistic effective core potential of 60 electrons was used to describe the core electrons of Au (*37, 38*), without consideration of spin-orbit coupling effects. The method was selected based on recommendations of its use for third-row transition metal complexes (*39*) and specifically for closely related Au-complexes (*40*) together with its demonstrated suitability for excited state calculations (*41-44*). The employed PBE0/def2-TZVP combination has been previously utilized with success in studies of luminescent Cu- and Au-complexes (*28, 45, 46*). The accuracy of the PBE0 method was further validated for CMA1 by comparison with the hybrid-meta exchange M06 functional accounting for noncovalent interactions (*47*). The two methods produced nearly identical excitation energies. The molecular structures of CMA compounds obtained with DFT and TD-DFT calculations are consistent with the X-ray crystal structures (Fig. S10), confirming the accuracy of the calculations.

Vertical transition energies were estimated by constraining the excited singlet to the ground state geometry (S_1^{P*}), while the S_1^P and T_1^R energies were estimated by fixing the dihedral angle and allowing the rest of the molecule to relax. For S_1^P, this simulates vibrational relaxation in a constrained geometry, as implicated in solid films. The relative state energies are presented in Table S4.

Vibrational frequencies were calculated for CMA1 to confirm the nature of the stationary points. S_0, S_1^R, T_1^P and T_1^R states were confirmed as minima in the potential energy surface. S_1^P was confirmed as a transition state, the imaginary frequency corresponding to ligand rotation. Excited state vibrational frequency calculations were carried out by TURBOMOLE version 6.3 (*48*). All other calculations were carried out by Gaussian 09 (*49*). Cartesian coordinates for these geometries are given in Table S5.

Cryogenic ns-µs time-resolved photoluminescence measurements

The solid-state samples for PL studies were spin-coated from anhydrous tetrahydrofuran solutions (10 mg/mL) onto pre-cleaned quartz substrates. The samples were placed under high vacuum for 15 min to remove the solvent. Time-resolved PL spectra were recorded using an electrically-gated intensified CCD (ICCD) camera (Andor iStar DH740 CCI-010) connected to a calibrated grating spectrometer (Andor SR303i). Photoexcitation was provided by femtosecond laser pulses which were created by second harmonic generation (SHG) in a BBO crystal from the fundamental output (pulse energy = 1.55 eV, pulse width = 80 fs) of a Ti:Sapphire laser system (Spectra Physics Solstice), at a repetition rate of 1 kHz. The photons from the laser pulses had a wavelength of 400 nm. A 420 nm long-pass filter was used to prevent scattered laser signal from entering the camera. Temporal evolution of the PL emission was obtained by stepping the ICCD gate delay with respect to the excitation pulse. The minimum gate width of the ICCD was

~2.5 ns. The cooling of the samples was provided by liquid helium, and the temperature of the samples was regulated using a temperature-controlled cryostat.

Ultrafast (fs-ps) transient grating photoluminescence measurements

A Ti:Sapphire amplifier system (Spectra-Physics Solstice) operating at 1 KHz generating 80-fs pulses was split into the pump and probe beam arms. The pump beam was generated by second harmonic generation (SHG) in a BBO crystal and focused onto the sample. The excitation density was 1×10^{19} cm^{-3} for thin films, excitation fluence was 300 μJ cm^{-2} for solutions. Photoluminescence is collimated using a silver off-axis parabolic mirror and focused onto the gate medium. About 80 μJ/pulse of the 800 nm laser output is used for the gate beams, which is first raised 25 mm above the plane of the PL to produce a boxcar geometry and split into a pair of gate beams using a 50/50 beam splitter. The gate beams are focused onto the gate medium (fused silica), crossing at an angle of ~5° and overlapping with the focused PL. The two gate beams interfere and create a transient grating in the gate medium due to a modulation of the refractive index via the optical Kerr effect. Temporal overlap between the two gate beams is achieved via a manual delay stage. The PL is then deflected on the transient grating causing a spatial separation of the gated signal from the PL background. Two lenses collimate and focus the gated signal onto the spectrometer entrance (Princeton Instruments SP 2150) after long- and short-pass filters remove scattered pump and gate light, respectively. Gated PL spectra are measured using an intensified CCD camera (Princeton Instruments, PIMAX4). The (~10 ns) electronic shutter of the intensified CCD camera was used to further suppress long-lived PL background. PL spectra at each gate time delay are acquired from ~10000 laser shots. The time delay between pump and gate beams is controlled via a motorized optical delay line on the excitation beam path and a LabVIEW data acquisition program.

Transient absorption (TA) spectroscopy

The output of a Ti:Sapphire amplifier system (Spectra-Physics Solstice) operating at 1 KHz and generating 90-fs pulses was split into the pump and probe beam paths. The visible and near-infrared broadband probe beams were generated in home-built noncollinear optical parametric amplifiers. The 400 nm narrowband (10 nm full-width at half-maximum) pump beam was provided by a TOPAS optical parametric amplifier (Light Conversion). The transmitted pulses were collected with an InGaAs dual-line array detector (Hamamatsu G11608-512) driven and read out by a custom-built board from Stresing Entwicklungsbüro. The excitation density for the visible measurements was $5x10^{17}$ cm^{-3}. The excitation density for the near-infrared measurements was $1x10^{19}$ cm^{-3}.

Raman Spectroscopy

Raman measurements were conducted by back-scattering (HORIBA T64000) a 532 nm (CW diode) line with a subtractive triple-stage. Spectra were collected between 18 and 1700 cm^{-1} where the CCD detector (HORIBA Synapse Open-Electrode) has a monotonically increasing quantum efficiency of between 0.43 and 0.50. Acquisitions employed a 100× optical objective and used minimal laser intensity to avoid laser damage. Powder samples were measured in air at room-temperature.

Fabrication of solution-processed OLEDs

Indium tin oxide (ITO)-coated glass substrates were cleaned with acetone (10 min) and isopropanol (10 min) in an ultrasonic bath. The substrates were blown dry using an N_2 flow gun, followed by O_2 plasma etching for 10 min. Poly(3,4-ethylenedioxythiophene):polystyrene sulfonate (PEDOT:PSS, Clevios P VP AI 4083) was filtered and spin-coated onto the substrates in air to form a ~30 nm layer, and was annealed at 200 °C for 15-30 min under nitrogen atmosphere. TFB (Cambridge Display Technology) was spin-coated from anhydrous toluene (Sigma-Aldrich) solution onto the PEDOT:PSS to form a layer of ~180 nm, followed by annealing at 200 °C for 20 min. The emissive layer was spin-coated from anhydrous dimethylformamide (Sigma-Aldrich) solution onto the TFB surface to achieve a ~20 nm layer. The weight concentration of CMA emitters in PVK (Sigma-Aldrich) was ~20%. This was followed by annealing at 90 °C for 10 min. ~70 nm thick BPhen (97%, Sigma-Aldrich) was then spin-coated from anhydrous methanol (Sigma-Aldrich) onto the emissive layer, followed by annealing at 60 °C for 10 min. Lithium fluoride (99.99%, Sigma-Aldrich) (0.6 nm) and aluminium (100 nm) were successively evaporated onto the samples through a shadow mask in a thermal evaporator under high vacuum ($< 3\times10^{-6}$ mbar), resulting in a device area of about 5.25 mm^2. After the assembly of electrical contacts, the devices were encapsulated under glass and stored in N_2 for 12-48 h before testing.

OLED performance characterization

The EL spectra of the devices were recorded using the calibrated ICCD-spectrometer set-up used in the PL measurements. The accuracy of the spectral data was cross-checked against a Labsphere CDS-610 spectrometer, as well as a Minolta CS-1000 luminance meter. Current density-voltage-luminance (J-V-L) characteristics were measured using a Minolta CS-200 luminance meter and a Keithley 2400 source-meter. The EQE of the devices were calculated based on the Lambertian emission profile measured. In addition, the accuracy of the EQE measurements for a subset of devices was checked using a calibrated silicon photodiode with known spectral response function, a Minolta CS-1000 luminance meter, as well as an integrating sphere. The histogram represents many batches of samples based on CMA4, with controlled layer thicknesses varied within ±20% of those specified above in order to empirically identify the optimum device structure.

Transient-electroluminescence measurements

The devices were electrically excited by a function generator using 1 kHz square voltage (current) pulses with a pulse width of 0.5 ms for the on-cycles (forward bias). The off-cycles of the device operation were provided by a reverse bias of -4 V to reduce charge accumulation effects. The instrument response time of the function generator was ~10 ns. The transient-EL of the samples was recorded by the same ICCD spectrometer used in the PL measurements.

Supplementary Text

Rate equations for the calculation of activation energy

We consider the excited state kinetics for a general organic emitter with intersystem crossing between singlet and triplet states. In this analysis, we focus on the delayed emission, for which the initial excited state population (after prompt emission and ISC) primarily comprises triplets in the T_1 state. This is consistent with reverable quenching of the delayed photoluminescence by exposure to oxygen. The kinetics of the delayed PL is therefore primarily governed by the temporal evolution of the triplet population.

The singlet decay processes are characterised by k_r^S (radiative decay of singlets) and k_{nr}^S (non-radiative decay of singlets). Similarly, in this model, k_r^T (radiative decay of triplets) and k_{nr}^T (non-radiative decay of triplets) are assumed to be possible in the triplet decay channels.

Conversion from singlets to triplets is characterised by the intersystem crossing (ISC) rate k_{ISC}, while the reverse process (RISC) is given by k_{RISC}. The kinetics of the singlet and triplet populations can be described by the following equations:

$$\frac{d[S]}{dt} = (-k_r^S - k_{nr}^S - k_{ISC})[S] + k_{RISC}[T] \quad \text{(S1)}$$

$$\frac{d[T]}{dt} = (-k_r^T - k_{nr}^T - k_{RISC})[T] + k_{ISC}[S] \quad \text{(S2)}$$

where [*S*] and [*T*] are singlet and triplet populations, respectively. During the delayed PL process (t >> 1 ns), the singlet population is small and varies much more slowly than $\left(k_r^S + k_{nr}^S + k_{ISC}\right)$. Therefore, the relation $\frac{d[S]}{dt} \approx 0$ can be assumed. Setting Eqn. S1 to zero, yields:

$$(-k_r^S - k_{nr}^S - k_{ISC})[S] + k_{RISC}[T] = 0 \quad \text{(S3)}$$

which can be rearranged to:

$$[S] = \frac{k_{RISC}}{k_r^S + k_{nr}^S + k_{ISC}}[T] \quad \text{(S4)}$$

Substitute Eqn. S4 into Eqn. S2, we obtain:

$$\frac{d[T]}{dt} = (-k_r^T - k_{nr}^T - k_{RISC})[T] + \frac{k_{ISC}k_{RISC}}{k_r^S + k_{nr}^S + k_{ISC}}[T] \quad \text{(S5)}$$

Therefore, under these assumptions the decay rate constant of the delayed emission $k_{delayed}$, is given by

$$k_{delayed} = k_r^T + k_{nr}^T + k_{RISC}(1 - \frac{k_{ISC}}{k_r^S + k_{nr}^S + k_{ISC}}) \quad \text{(S6)}$$

In principle, both k_{ISC} and k_{RISC} may be thermally accelerated, e.g. through the promotion of molecular rotation. We examine below which is dominant. For simplicity, we assume the rates of the other decay processes remain constant.

Eqn. S6 can be re-written as:

$$k_{delayed} = k_r^T + k_{nr}^T + k_{RISC} - \frac{k_{RISC}}{\frac{k_r^S + k_{nr}^S}{k_{ISC}} + 1} \quad \text{(S7)}$$

According to Eqn. S7, if k_{ISC} is the dominant temperature-dependent process, increasing temperature will result in a lower k_{delayed}, which corresponds to longer lifetime of the delayed PL. By contrast, if k_{RISC} is the dominant temperature-dependent process, Eqn. S6 predicts a higher k_{delayed} as the temperature increases. The latter agrees with experiment (Fig. 2A) so we conclude k_{RISC} is the dominant temperature-dependent process. In contrast to mechanistically similar process TADF, the thermal energy discussed here is that required to overcome the rotational barrier between the planar triplet and lower-lying rotated states.

We define a temperature-independent triplet decay rate constant

$$k_0 = k_r^T + k_{nr}^T \quad \text{(S8)}$$

and a temperature-independent coefficient

$$\alpha = 1 - \frac{k_{ISC}}{k_r^S + k_{nr}^S + k_{ISC}} \quad \text{(S9)}$$

By inspecting Eqn. S9, it is clear that α is a constant between 0 and 1.

The temperature-dependent part of Eqn. S6 can then be written as

$$k_T = \alpha k_{RISC} \quad \text{(S10)}$$

which corresponds to the temperature-dependent emission rate described in the main text.

Then Eqn. S6 can be simplified to

$$k_{delayed} = k_0 + k_T \quad \text{(S11)}$$

Therefore, the function to describe the delayed PL process can be written as

$$PL_{delayed} = PL_{delayed0} e^{-(k_0 + k_T)t} \quad \text{(S12)}$$

where $PL_{delayed}$ and PL_{delayed0} are the intensity and the initial (t = 0) intensity of the delayed PL component respectively.

Assume the temperature-dependent rate constant has the form

$$k_T = \beta e^{-\frac{E_A}{k_B T}} \quad \text{(S13)}$$

where E_A is the thermal activation energy, k_{B} is Boltzmann constant, T is the temperature in Kelvin and β is a constant.

Therefore, we have:

$$\ln(k_T) = -(\frac{E_A}{k_B})(\frac{1}{T}) + C \quad \text{(S14)}$$

Supplementary Figures

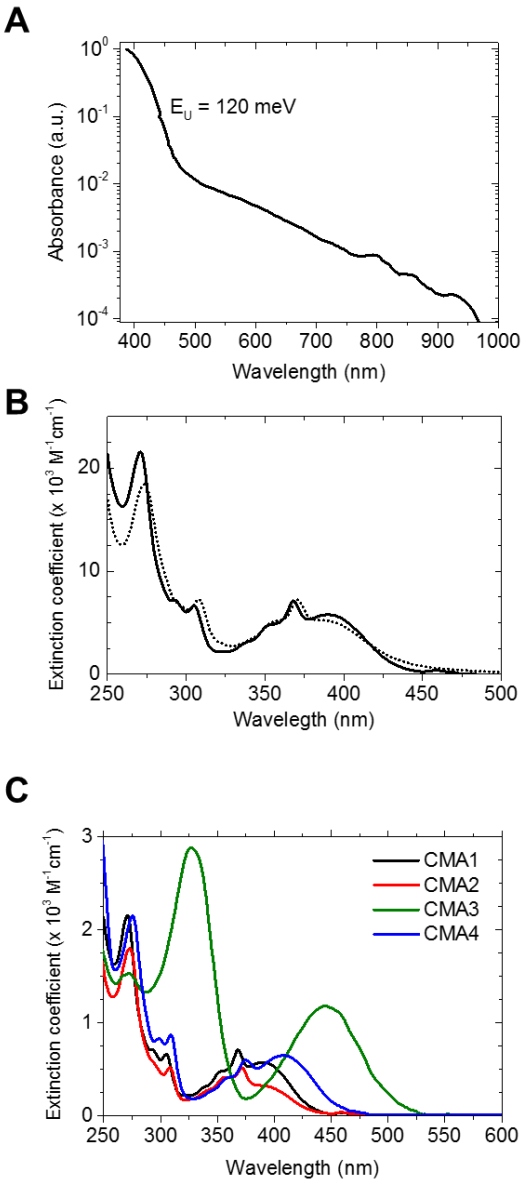

Fig. S1 Additional absorption data. A) Photothermal deflection spectrum of CMA1 spin-cast film indicating the Urbach tail with characteristic energy E_U (120 meV) and a slowly varying background absorption extending to the near-IR. **(B)** Molar extinction of CMA1 in THF solution (solid) and absorption in neat solid film (dot) including UV region. To convert from molar extinction (M^{-1} cm^{-1}) to film absorption (cm^{-1}), multiply by 2. **(C)** Molar extinction coefficient of CMA1-4 in THF solution.

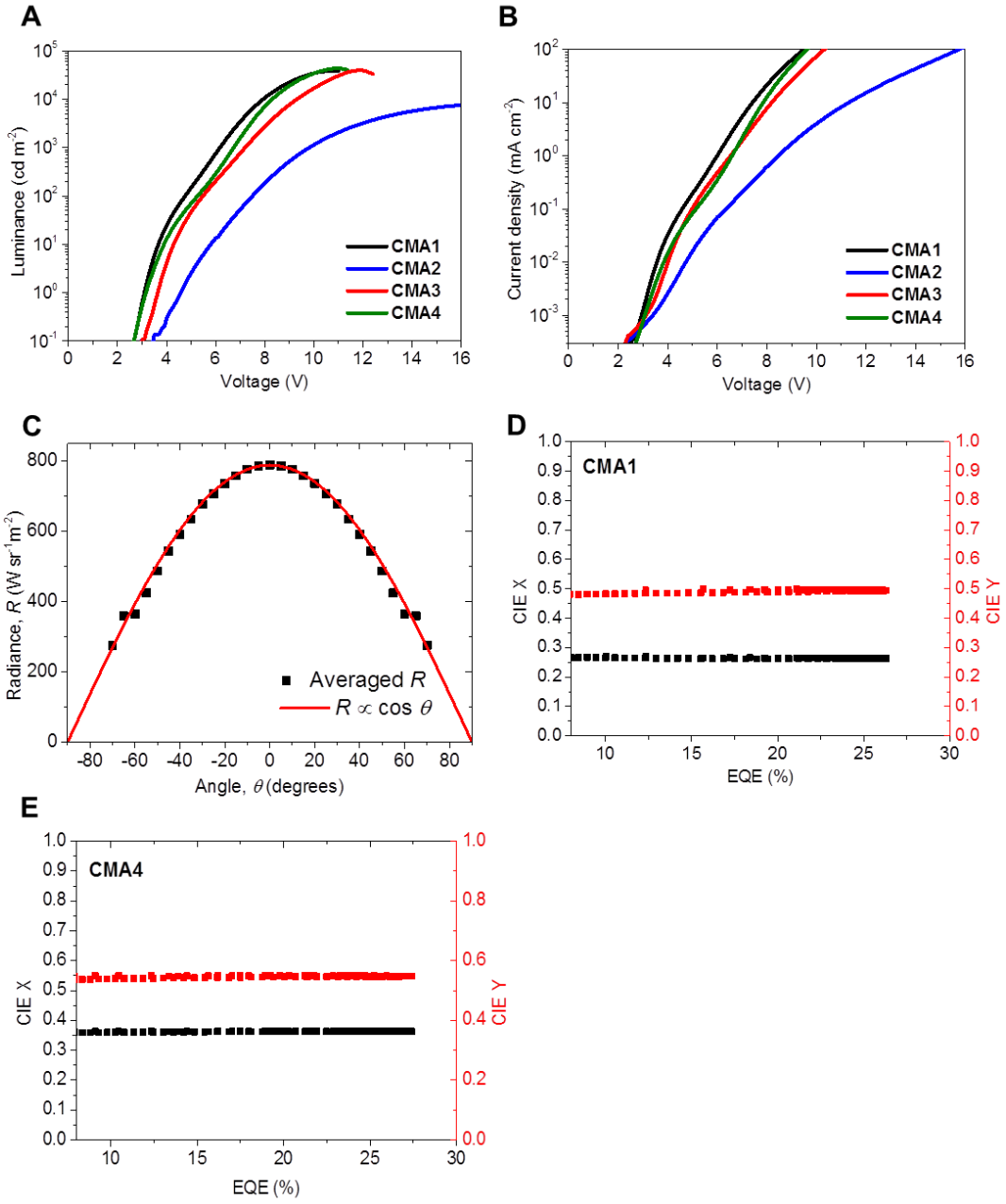

Fig. S2 Additional device performance data. (A) Luminance versus voltage. **(B)** Current density versus voltage. **(C)** Angular emission profile of a representative device, consistent with Lambertian emission characteristics as fitted by the red line. **(D), (E)** CIE coordinates as a function of EQE for OLEDs fabricated from CMA1 and CMA4. All devices utilize 20 wt% CMA in PVK host, device area 5.25 mm^2.

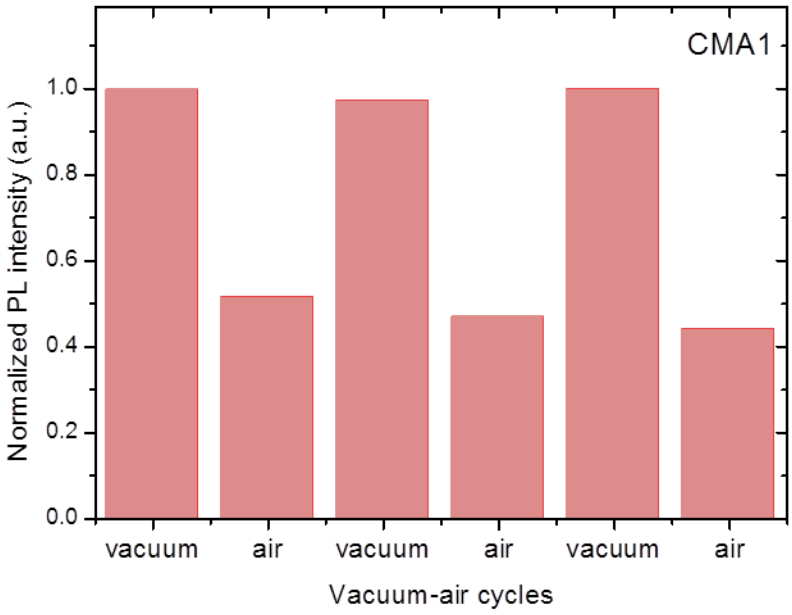

Fig. S3 Reversible PL quenching by exposure to oxygen for CMA1. Change in PL intensity of a thin film of CMA1 under sequential (left to right) vacuum-air cycles, normalized to the intensity of the first measurement. Vacuum of $< 10^{-5}$ mBar, achieved using a turbomolecular pump. Samples stabilized for 10 minutes under vacuum or in air prior to each measurement. The reversibility implicates triplets in the luminescence pathway, since these can quench by transfer to the triplet ground state of molecular oxygen.

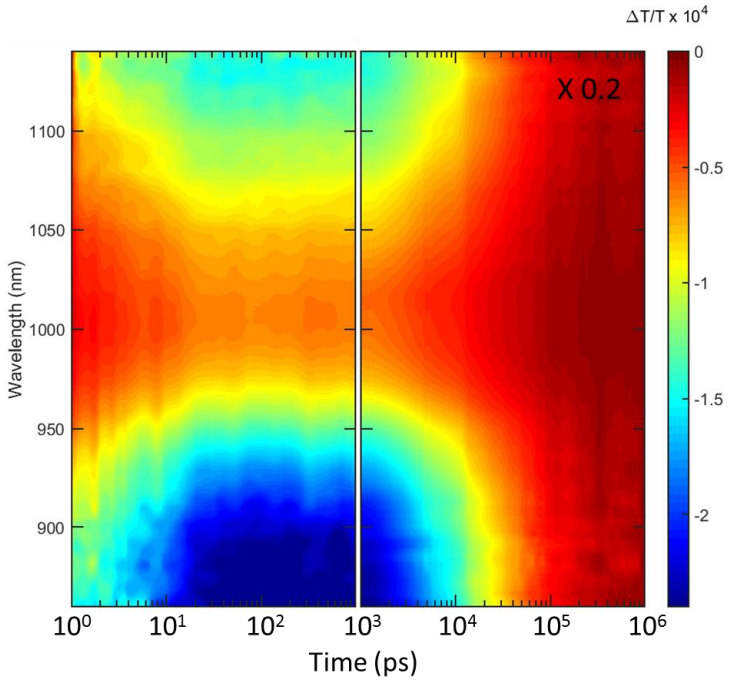

Fig. S4 Near-Infrared transient absorption data for CMA1. TA of neat CMA1 film on ps-µs timescales, 400nm pump, excitation density 1×10^{19} cm^{-3}. There are no NIR features associated with the singlet, but two PIA features at ~860 nm and > 1050 nm have identical growth and decay kinetics to the 645 nm triplet PIA seen in Fig. 2D at the same excitation density.

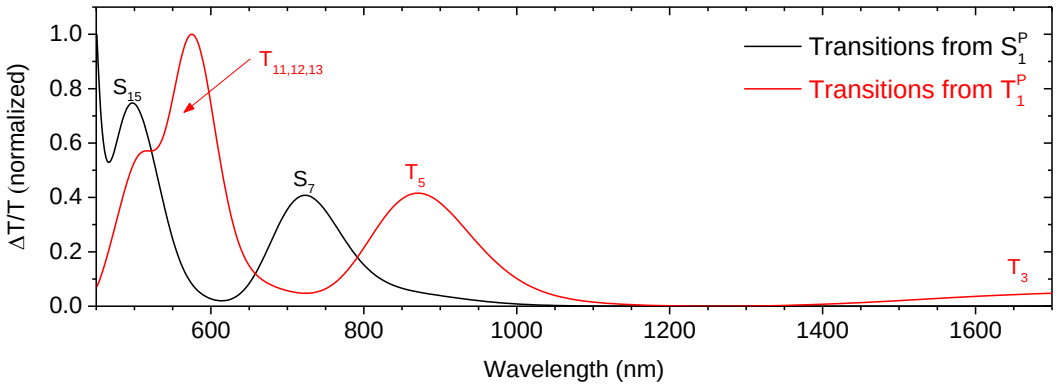

Fig. S5 Calculated PIA spectra for CMA1 in co-planar geometry. Excited state transitions from S_1/T_1 to S_n/T_n for CMA1 considering the first 20 singlet and triplet excited states in the co-planar geometry, from TD-DFT calculations. Each transition is weighted by its calculated oscillator strength and a Gaussian broadening of 150 meV is assumed. Within the available measurement range, 2-3 triplet PIA features are expected and 1-2 singlet PIA features, with the $S_1 \rightarrow S_7$ transition bracketed by two of the triplet PIAs. Tabulated data are presented in Table S6.

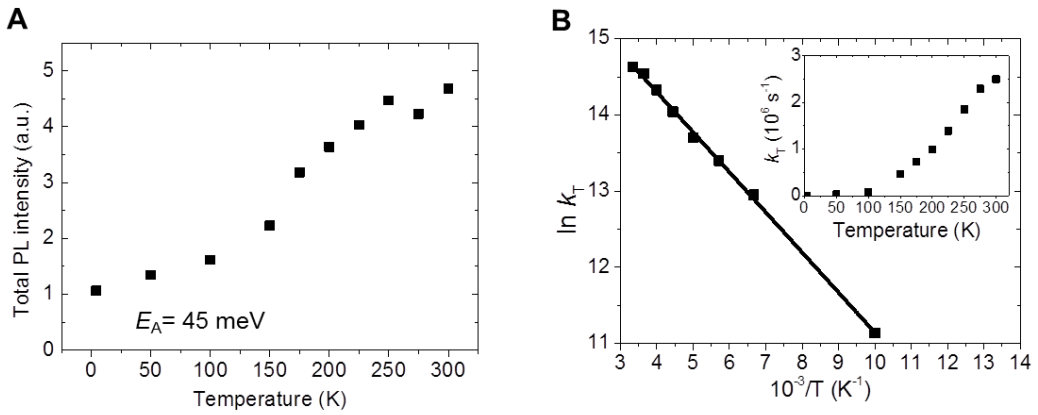

Fig. S6 Additional temperature-dependent PL of CMA1 neat film. (A) Temperature-dependent total PL intensities calculated by integrating the time-dependent decays over the complete measurement window. **(B)** Temperature-dependent decay rate k_T, showing an activation energy of 45 meV above 100K.

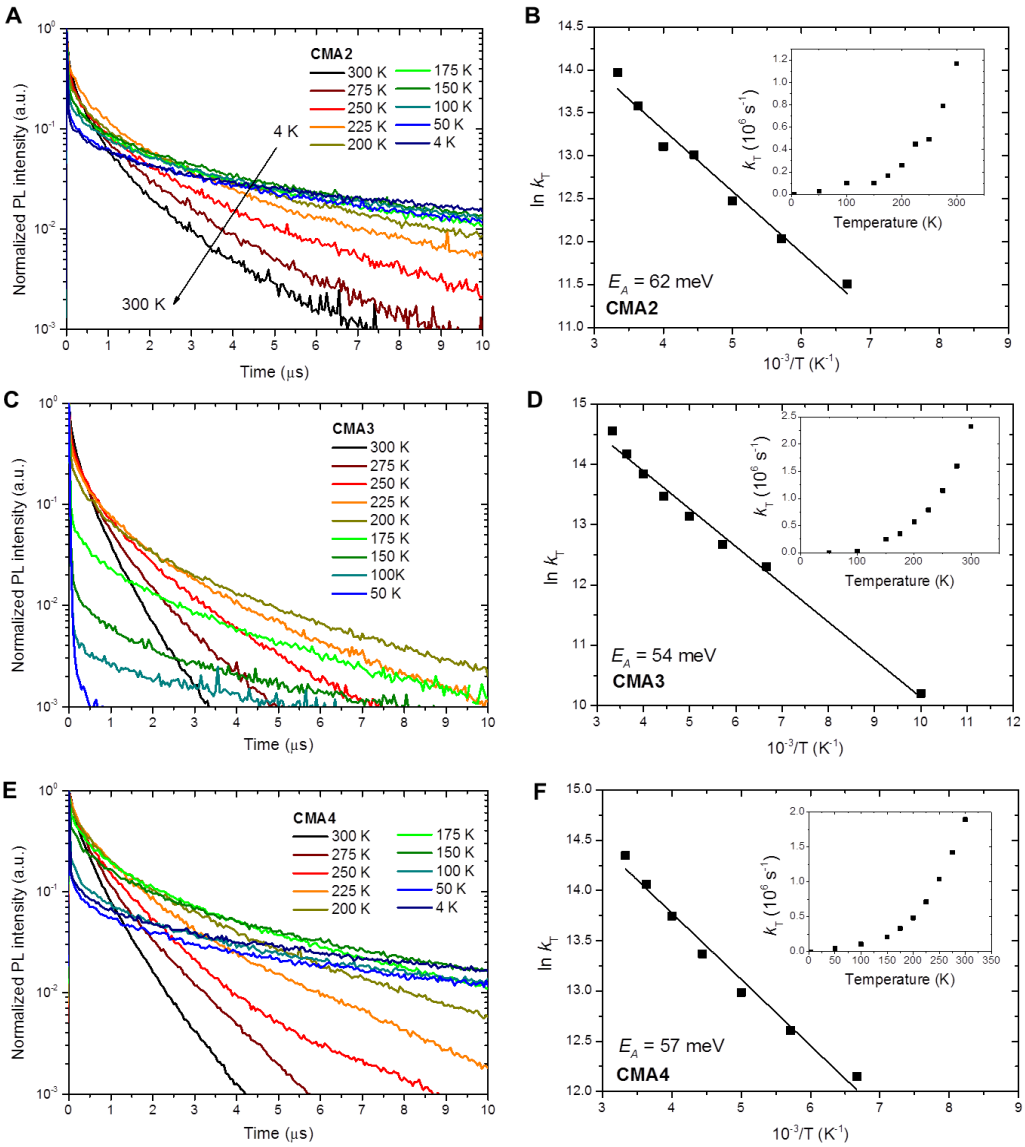

Fig. S7 Transient photoluminescence characterization of CMA2-4. (A, C, E) Temperature-dependent ns-μs PL kinetics measured using an electrically gated ICCD for neat films of CMA2-4. **(B, D, F)** Activation energies for the rate of delayed emission from CMA2-4.

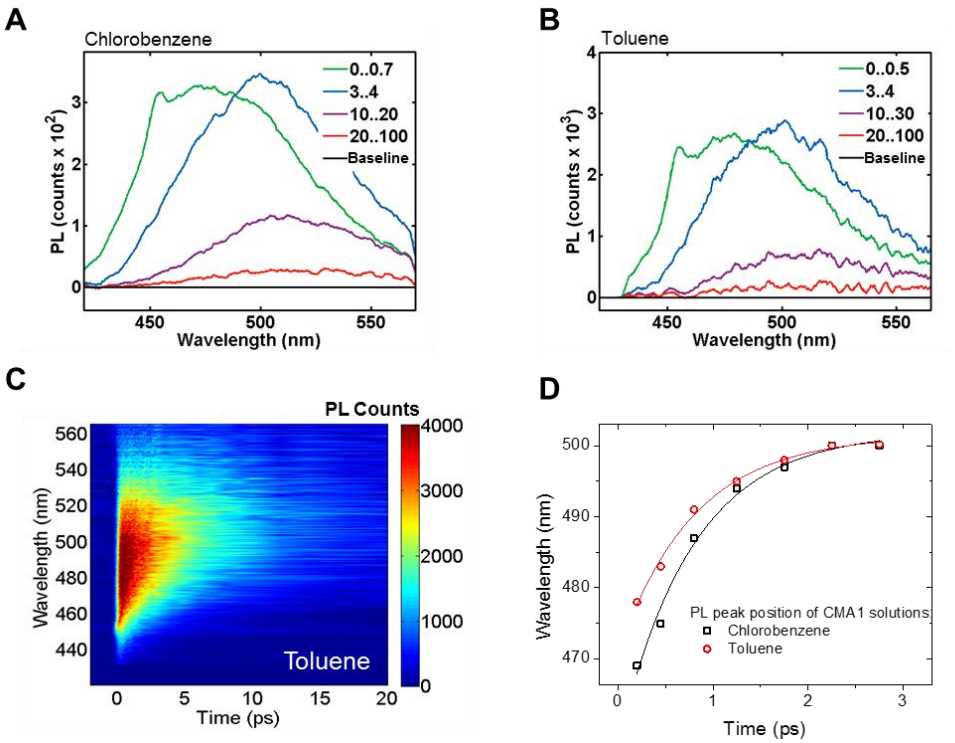

Fig. S8 Transient PL measurements of CMA1 in solutions. (**A**) Kerr-gated PL spectra of CMA1 dissolved in chlorobenzene. (**B**) Kerr-gated PL spectra of CMA1 dissolved in toluene. (**C**) Ultrafast PL map of CMA1 in toluene. (**D**) Peak position shift over time for CMA1 in chlorobenzene (black squares) and toluene (red circles) with exponential fits as guides to the eye. The initial shift is slightly faster in toluene, but the final emission and decay rate are nearly identical for both solvents.

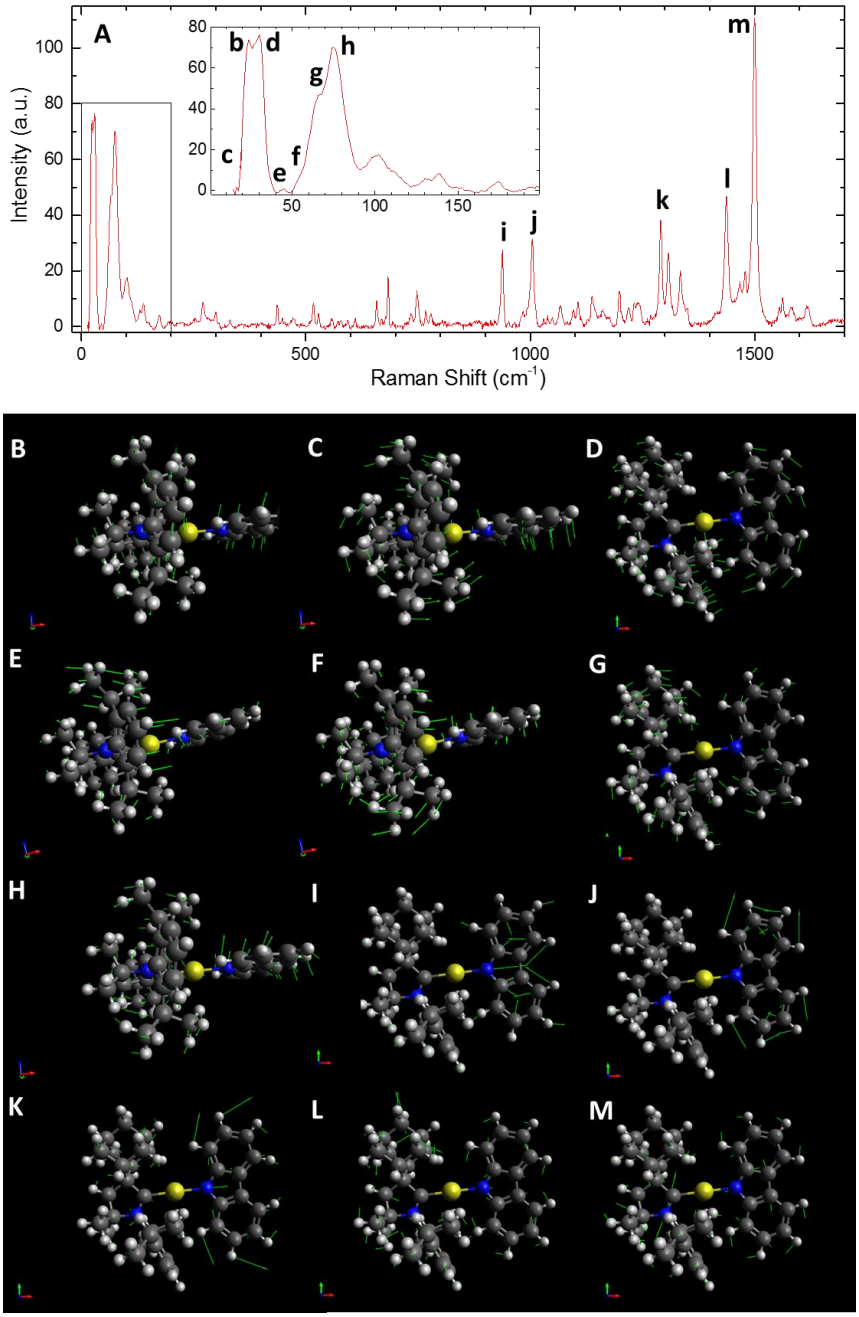

Fig. S9 Experimental Raman spectrum of solid CMA1 and primary Raman-active normal modes from DFT calculations. Relative atomic motion indicated by green arrows. **(A)** Measured Raman spectrum, inset highlights the cluster of low-frequency modes with high Raman activity. b-m correspond to peaks assigned to modes B-M. **(B)** relative rotation of carbene and amide about the axis of the C-M-A linkage, calculated frequency 21.41 cm^{-1}. **(C, D, G, H)** relative rotation of carbene and amide about other axes, calculated frequencies 20.80 cm^{-1}, 27.46 cm^{-1}, 69.86 cm^{-1}, 82.68 cm^{-1}. **(E, F)** relative rotation of substituted phenyl group on amide moiety, calculated frequencies 48.19 cm^{-1}, 54.11 cm^{-1}. **(I, J, K, L, M)** vibrational and "ring stretch" modes, calculated frequencies 956.69 cm^{-1}, 1045.93 cm^{-1}, 1328.29 cm^{-1}, 1483.38 cm^{-1}, 1542.32 cm^{-1}.

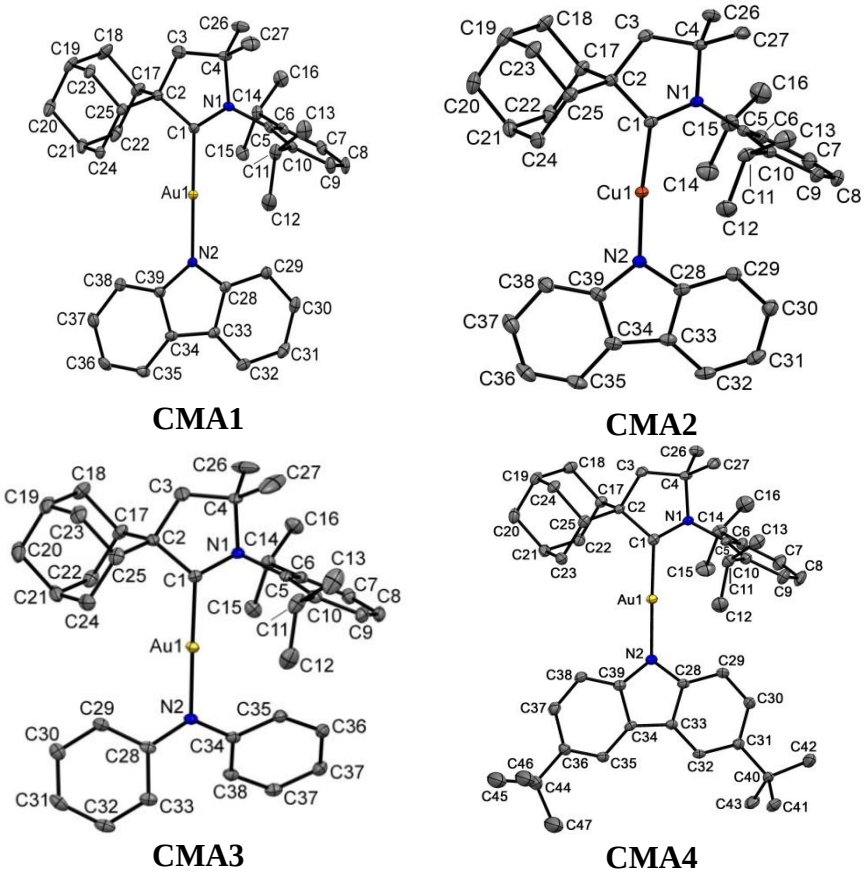

Fig. S10 Crystal structures of (CAAC)AuCz (CMA1), (CAAC)CuCz (CMA2), (CAAC)AuNPh$_2$ (CMA3) and (CAAC)AuDTBCz (CMA4). Ellipsoids are shown at the 50% level. Hydrogen atoms are omitted for clarity. Selected bond lengths (Å) and angles (°): CMA1: Au1–C1 1.991(3), Au1–N2 2.026(2), C1–C2 1.528(4), C1–N1 1.299(4), N2–C28 1.379(4), N2–C39 1.381(4), C1–Au1–N2 178.78(11); dihedral angle between best planes C1-C2-C3-C4-N1 (CAAC) and C28-N2-C39-C33-C34 (carbazole) = 16.5°. CMA2: Cu–C1 1.8846(15), Cu–N2 1.8626(14), C1–C2 1.527(2), C1–N1 1.305(2), C1–Cu–N2 174.34(6); dihedral angle between best planes C1-C2-C3-C4-N1 and C28-N2-C39-C33-C34 = 2.8°. CMA3: Au1–C1 1.985(2), Au1–N2 2.040(2), C1–C2 1.532(3), C1–N1 1.304(3), N2–C28 1.393(3), N2–C34 1.401(3), C1–Au1–N2 177.27(9); dihedral angle between best plane C1-C2-C3-C4-N1 (CAAC) and C28-N2-C34 = 14.9°. CMA4: Au1–C1 1.997(3), Au1–N2 2.020(2), C1–C2 1.536(4), C1–N1 1.307(4), N2–C28 1.395(4), N2–C39 1.384(4), C1–Au1–N2 178.25(11); dihedral angle between best planes C1-C2-C3-C4-N1 (CAAC) and C28-N2-C39-C33-C34 (carbazole) = 14.7°.

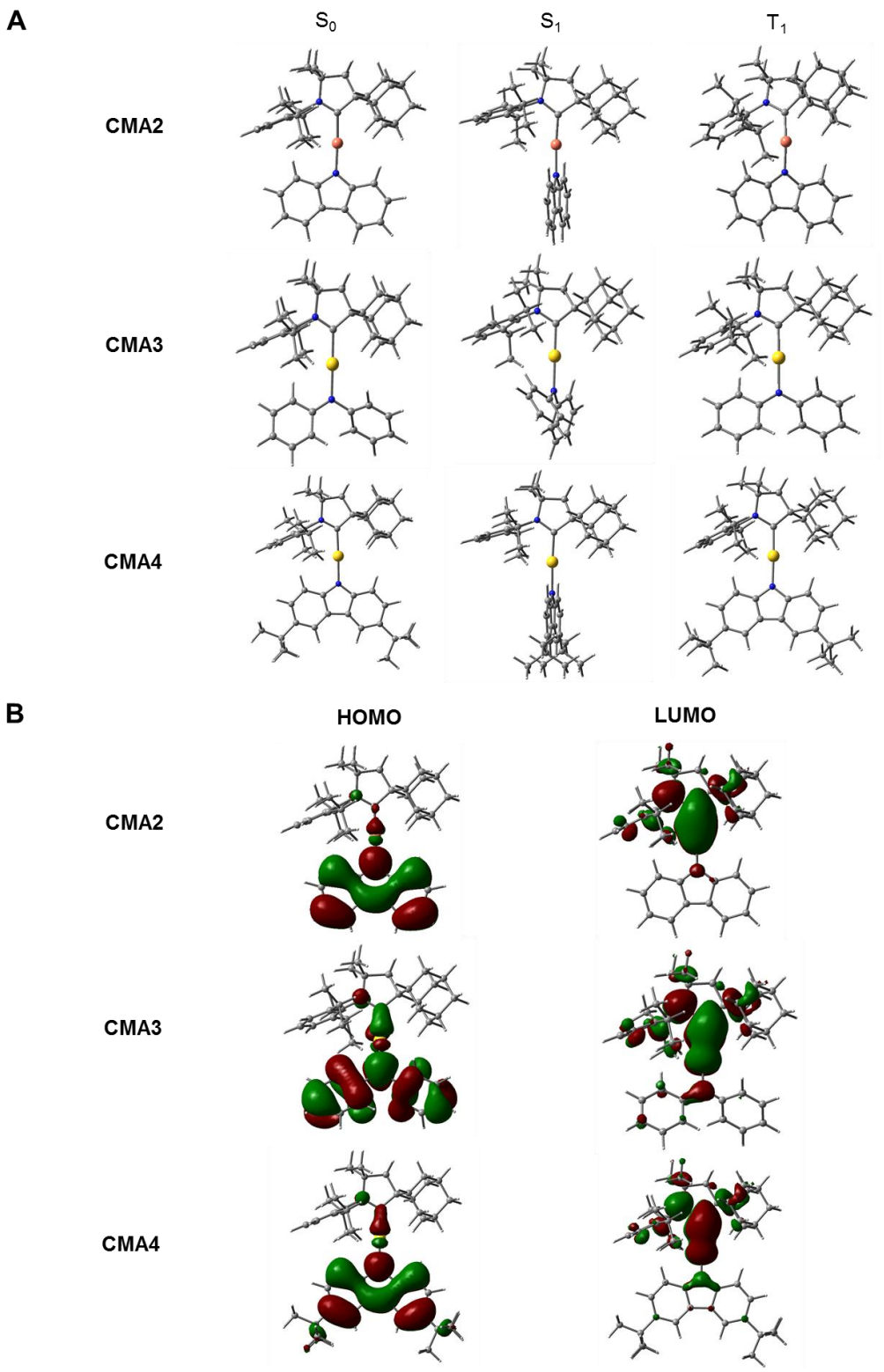

Fig. S11 DFT and TD-DFT calculations for CMA2-4. (A) Optimized molecular geometries for S_0, S_1, and T_1. **(B)** HOMO and LUMO wave functions, isovalue = 0.02 $(\text{electrons/bohr}^3)^{1/2}$.

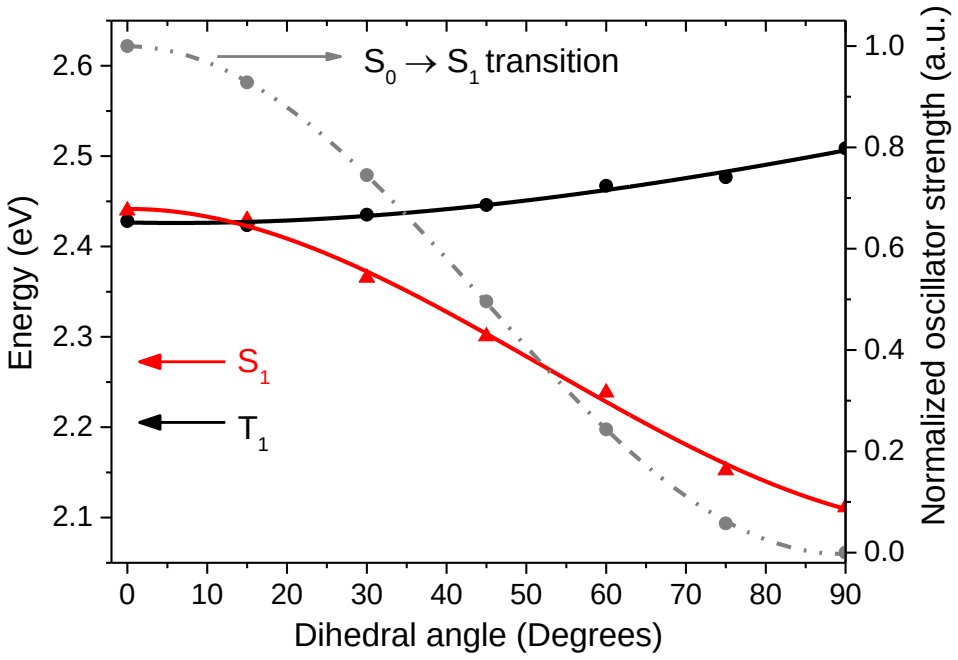

Fig. S12 Variation of energy and oscillator strength with dihedral angle for CMA1. Variation of S_1 and T_1 energies and normalized oscillator strength of the $S_0 \rightarrow S_1$ transition obtained from TD-DFT calculations for CMA1, after geometric relaxation with the carbene-amide dihedral angle fixed. By comparison with spectroscopy, the calculated singlet energies are underestimated by 5-10%, whereas the lowest triplet energy accurately predicts the phosphorescence. Accounting for this discrepancy increases the dihedral angle at which singlet and triplet are degenerate, from approximately 15° to approximately 45°. Solid lines are polynomial (energy) and sinusoidal (oscillator strength) fits as guides to the eye.

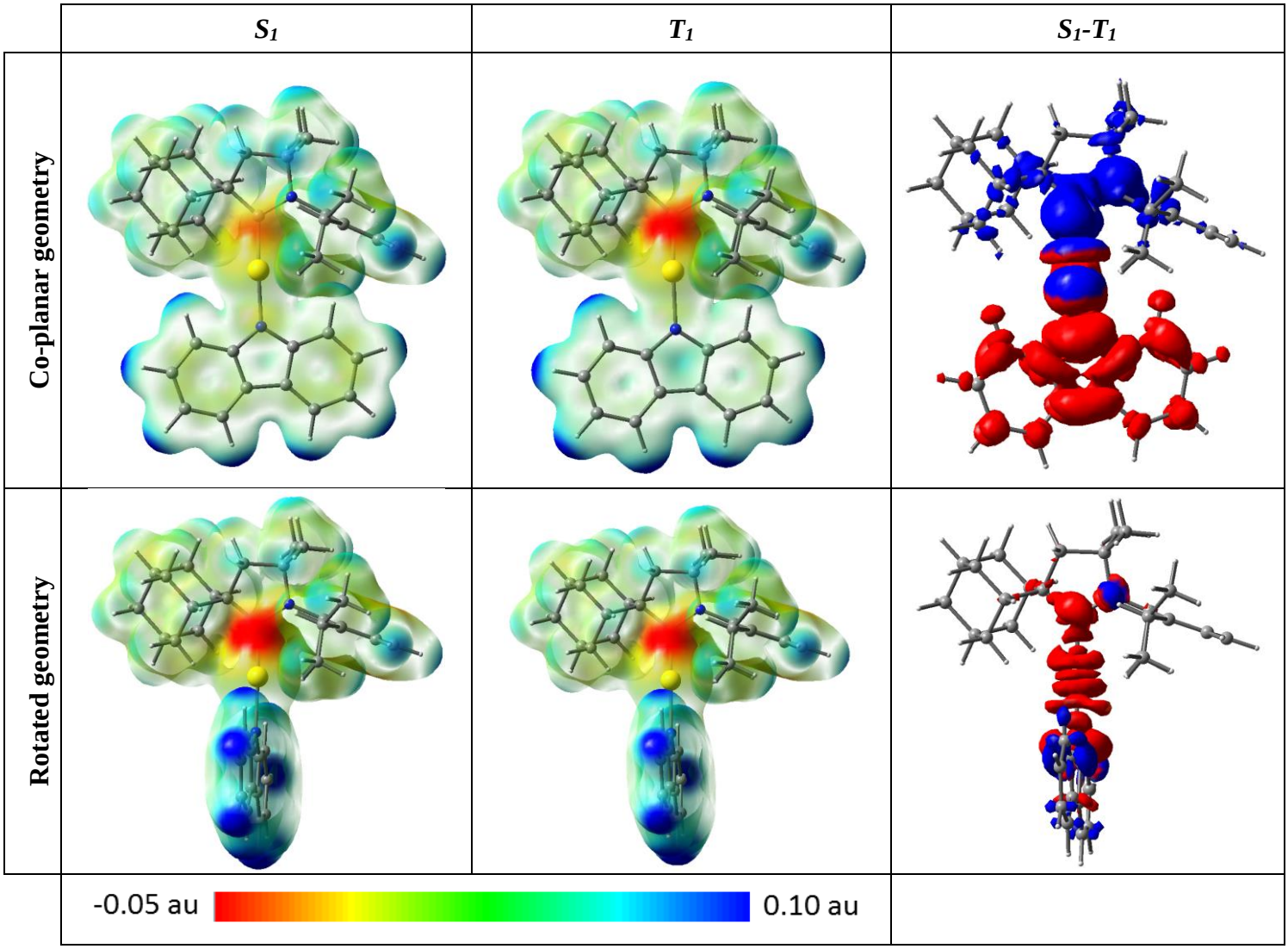

Fig S13 Electrostatic potential energy maps for the excited S_1 and T_1 states from TD-DFT calculations. Isodensity = 0.01 e/au^3**.** The right column presents a subtraction to illustrate areas which are relatively more electron rich for S_1 (red) and T_1 (blue). For comparison in the co-planar geometry, the relaxed T_1 geometry is used (using the S_1^P geometry yields very similar maps). For the rotated geometry, the relaxed S_1 geometry is used.

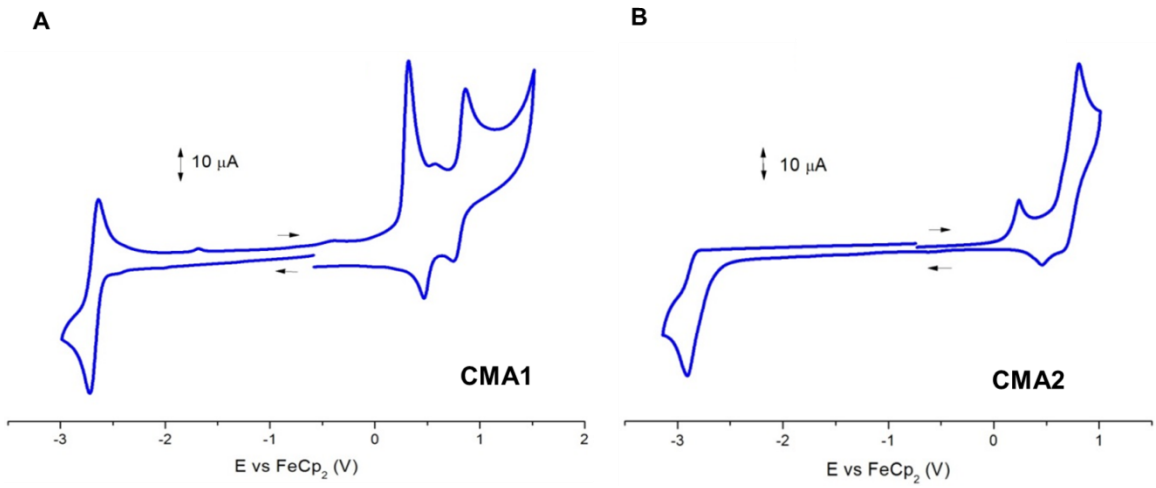

Fig. S14 Cyclic voltammogram. (A) CMA1. **(B)** CMA2. Data was recorded using a glassy carbon electrode in MeCN solution with [n-Bu_4N]PF_6 as supporting electrolyte with a scan rate of 0.1 V s^{-1}.

Table S1 Decomposition temperatures for CMA1-4 by thermal gravimetric analysis (TGA).

Compound	T_d (°C)
CMA1	334
CMA2	303
CMA3	271
CMA4	336

Table S2 Formal electrode potentials for CMA1-4. Formal electrode potentials ($E_{1/2}$ for irreversible and quasi-reversible processes (*) *vs*. $FeCp_2$), onset potentials (E *vs*. $FeCp_2$), E_{HOMO}/E_{LUMO} (eV) and band gap values (E_g, eV) for the redox changes exhibited by the complexes under study in MeCN solution (1.4 mM), supporting electrolyte [n-Bu_4N][PF_6] (0.13 mol dm^{-3}), measured at 0.1 V $\mathbf{s^{-1}}$. $E_{HOMO} = -(E_{onset\ ox\ Fc/Fc+} + 5.39)$ eV, based on first oxidation potential, and $E_{LUMO} = -(E_{onset\ red\ Fc/Fc+} + 5.39)$ eV, based on first reduction potential. Cyclic voltammetry of CMA1 and CMA2 are shown in Fig. S14.

Compound	Reduction (V)		E_{LUMO} (eV)	Oxidation (V)			E_{HOMO} (eV)	E_g (eV)
	$E_{M(I)/M(0)}$	$E_{onset\ red}$		E_{1st}	$E_{onset\ ox}$	E_{2nd}		
CMA1	–2.68*	–2.60	–2.79	+0.26	+0.22	+0.77	–5.61	2.82
CMA2	–2.84*	–2.73	–2.66	+0.12	+0.07	+0.71	–5.46	2.80
CMA3	–2.78*	–2.69	–2.70	–0.13	–0.17	+0.49	–5.22	2.52
CMA4	–2.86*	–2.78	–2.61	+0.13	+0.08	+0.65	–5.47	2.86

Table S3 Comparison of molecular structural features obtained experimentally by X-ray crystallography and by DFT calculation for CMA1.

	Experimental (X-ray crystallography)	DFT Calculation
Au–C	1.994Å	1.991Å
Au–N	2.027Å	2.015Å
C–Au–N	178.7°	178.0°

Table S4 TD-DFT calculation of excited state energies for CMA1-4. S_1^R and T_1^P are fully relaxed states. S_1^P and T_1^R are calculated by allowing geometric relaxation while keeping the carbene-amide dihedral angle fixed at 0° and 90°, respectively. S_1^{P*} and T_1^{P*} are constrained to the ground state geometry.

Compound	S_1^R **(eV)**	T_1^P **(eV)**	$S_1^R - T_1^P$ **(eV)**	S_1^{P*} **(eV)**	T_1^{P*} **(eV)**	S_1^P **(eV)**	T_1^R **(eV)**
CMA1	2.11	2.43	-0.32	2.63	2.69	2.44	2.51
CMA2	2.05	2.39	-0.34	2.49	2.67	2.21	2.40
CMA3	1.81	2.05	-0.24	2.47	2.34	2.12	2.13
CMA4	1.99	2.29	-0.30	2.53	2.57	2.35	2.35

Table S5 Coordinates and stability characterization of CMA1 geometries from TD-DFT calculations.

S_0	S_1^P	S_1^R	T_1^P	T_1^R
Minimum	Transition state	Minimum	Minimum	Minimum
0 imaginary frequencies	1 imaginary frequency = carbazole rotation (i8.24cm^{-1})	0 imaginary frequencies	0 imaginary frequencies	0 imaginary frequencies
Cartesian coordinates:	Cartesian coordinates:	Cartesian coordinates:	Cartesian coordinates:	Cartesian coordinates:
Au 0.469 0.346 -0.082	Au 0.499 0.318 0.095	Au 0.581 0.222 -0.110	Au 0.494 0.416 -0.169	Au -0.580 -0.256 -0.143
N 2.471 0.569 -0.042	N 2.637 0.485 0.188	N 2.676 0.278 0.015	N 2.536 0.675 -0.028	N -2.640 -0.331 -0.010
C 4.580 1.486 0.003	C 4.752 1.366 -0.002	C 4.893 0.242 -0.613	C 4.650 1.582 -0.011	C -4.779 -0.500 0.831
C -0.782 -2.829 1.325	C -0.857 -2.908 1.283	C -1.551 -2.544 1.579	C -0.826 -2.775 1.264	C 1.480 2.488 1.679
N -1.999 -1.151 -0.012	N -2.063 -1.118 0.106	N -2.159 -0.958 -0.197	N -1.929 -1.241 -0.310	N 2.124 1.013 -0.182
C -2.477 2.108 -1.329	C -2.421 2.115 -1.441	C -1.902 2.442 -1.524	C -2.486 2.268 -1.151	C 1.949 -2.356 -1.607
H -2.353 1.567 -2.274	H -2.302 1.501 -2.341	H -1.665 1.921 -2.459	H -2.183 1.937 -2.151	H 1.691 -1.816 -2.525
C -1.451 3.809 0.195	C -1.354 3.888 -0.035	C -0.989 3.945 0.255	C -1.822 3.676 0.811	C 1.090 -3.929 0.139
H -0.581 4.453 0.355	H -0.466 4.519 0.087	H -0.095 4.471 0.609	H -1.039 4.323 1.223	H 0.212 -4.486 0.486
C -3.498 -1.242 -0.003	C -3.540 -1.100 0.179	C -3.593 -0.780 -0.491	C -3.380 -1.362 -0.543	C 3.561 0.883 -0.490
C -0.078 -4.029 1.359	C -0.172 -4.119 1.226	C -1.120 -3.816 1.943	C -0.057 -3.916 1.473	C 1.021 3.728 2.110
H 0.245 -4.423 2.315	H 0.163 -4.582 2.148	H -1.077 -4.079 2.995	H 0.124 -4.252 2.488	H 0.972 3.934 3.174
C -2.763 1.885 1.137	C -2.739 2.081 1.021	C -2.672 2.170 0.818	C -3.084 1.534 1.142	C 2.733 -2.129 0.735
H -2.835 1.193 1.983	H -2.839 1.461 1.916	H -2.978 1.464 1.596	H -3.211 0.684 1.818	H 3.030 -1.437 1.529
C 3.635 4.090 0.018	C 3.844 3.953 0.478	C 4.253 0.007 -3.308	C 3.721 4.097 -0.744	C -3.872 -0.989 3.410
H 3.281 5.116 0.025	H 3.515 4.969 0.658	H 4.031 -0.081 -4.364	H 3.383 5.086 -1.029	H -3.542 -1.184 4.424
C -1.501 0.058 -0.102	C -1.494 0.113 -0.129	C -1.406 0.213 -0.277	C -1.470 0.075 -0.215	C 1.405 -0.179 -0.287
C 3.392 -0.454 -0.034	C 3.489 -0.529 -0.098	C 3.442 0.403 1.139	C 3.422 -0.316 0.315	C -3.526 -0.162 -1.049
C -1.290 3.046 -1.118	C -1.201 3.021 -1.283	C -0.676 3.220 -1.051	C -1.423 3.209 -0.587	C 0.748 -3.179 -1.145
H -1.242 3.748 -1.958	H -1.104 3.655 -2.172	H -0.387 3.944 -1.823	H -1.311 4.072 -1.256	H 0.472 -3.890 -1.934
H -0.350 2.487 -1.123	H -0.291 2.417 -1.219	H 0.174 2.543 -0.915	H -0.457 2.695 -0.553	H -0.120 -2.529 -0.986
C 0.370 -1.573 3.153	C 0.310 -1.817 3.214	C -0.563 -1.156 3.397	C -0.131 -1.382 3.227	C 0.522 0.997 3.431
H 0.872 -0.936 2.422	H 0.814 -1.115 2.545	H 0.158 -0.772 2.673	H 0.431 -0.707 2.577	H -0.206 0.648 2.696
H 1.039 -2.404 3.387	H 0.970 -2.675 3.370	H -0.115 -2.012 3.909	H 0.552 -2.149 3.602	H 0.071 1.819 3.996
H 0.222 -0.993 4.068	H 0.167 -1.324 4.180	H -0.759 -0.379 4.142	H -0.491 -0.806 4.084	H 0.732 0.182 4.130
C -0.810 -2.984 -1.123	C -0.981 -2.917 -1.156	C -1.168 -3.132 -0.755	C -0.473 -3.034 -1.138	C 1.081 3.190 -0.620
C 0.243 -4.712 0.202	C 0.101 -4.734 0.019	C -0.739 -4.746 0.995	C 0.479 -4.628 0.415	C 0.621 4.700 1.212
H 0.792 -5.645 0.255	H 0.627 -5.682 -0.005	H -0.416 -5.736 1.298	H 1.060 -5.526 0.597	H 0.277 5.666 1.567
C -1.556 2.807 1.344	C -1.512 2.981 1.184	C -1.426 2.917 1.298	C -1.998 2.451 1.709	C 1.511 -2.919 1.206
H -1.682 3.338 2.294	H -1.628 3.586 2.091	H -1.646 3.417 2.249	H -2.281 2.766 2.720	H 1.753 -3.439 2.141
H -0.632 2.227 1.424	H -0.616 2.366 1.318	H -0.616 2.204 1.484	H -1.055 1.904 1.791	H 0.686 -2.232 1.420
C -2.719 4.658 0.130	C -2.591 4.772 -0.182	C -2.115 4.949 0.014	C -3.136 4.449 0.724	C 2.238 -4.898 -0.137
H -2.842 5.229 1.057	H -2.705 5.415 0.698	H -2.343 5.494 0.937	H -3.432 4.809 1.716	H 2.488 -5.461 0.770
H -2.645 5.383 -0.687	H -2.484 5.430 -1.052	H -1.803 5.691 -0.731	H -3.012 5.332 0.085	H 1.937 -5.629 -0.898
C 3.187 1.745 -0.018	C 3.371 1.627 0.226	C 3.539 0.191 -1.040	C 3.270 1.818 -0.224	C -3.394 -0.545 1.122
C -1.182 -2.341 0.070	C -1.300 -2.323 0.083	C -1.622 -2.211 0.211	C -1.083 -2.357 -0.060	C 1.560 2.230 0.294
C -2.639 1.069 -0.189	C -2.594 1.155 -0.232	C -2.363 1.377 -0.495	C -2.670 1.006 -0.269	C 2.393 -1.310 -0.553
C 0.267 -1.915 -3.108	C -0.057 -1.752 -3.170	C 0.437 -2.719 -2.622	C 0.840 -2.056 -3.033	C -0.536 2.843 -2.487
H 0.739 -1.162 -2.474	H 0.450 -1.023 -2.535	H 0.974 -2.011 -1.990	H 1.219 -1.261 -2.388	H -1.059 2.106 -1.875
H 0.091 -1.475 -4.092	H -0.310 -1.265 -4.116	H 0.536 -2.401 -3.664	H 0.778 -1.664 -4.053	H -0.644 2.561 -3.539
H 0.975 -2.739 -3.228	H 0.642 -2.565 -3.388	H 0.920 -3.696 -2.524	H 1.566 -2.874 -3.033	H -1.029 3.809 -2.348
C 5.798 -0.817 0.004	C 5.846 -0.955 -0.482	C 5.763 0.493 1.832	C 5.788 -0.671 0.663	C -5.902 -0.106 -1.493
H 6.813 -0.433 0.024	H 6.876 -0.628 -0.570	H 6.825 0.477 1.617	H 6.813 -0.321 0.692	H -6.936 -0.165 -1.173
C 3.167 -1.830 -0.047	C 3.176 -1.885 -0.255	C 3.002 0.546 2.455	C 3.127 -1.646 0.601	C -3.221 0.052 -2.389
H 2.157 -2.227 -0.065	H 2.152 -2.226 -0.166	H 1.944 0.570 2.677	H 2.104 -2.006 0.573	H -2.187 0.103 -2.709
C -3.748 2.965 -1.390	C -3.660 3.008 -1.586	C -3.028 3.457 -1.767	C -3.803 3.049 -1.236	C 3.098 -3.336 -1.887
H -3.663 3.664 -2.229	H -3.546 3.641 -2.474	H -2.707 4.172 -2.534	H -3.669 3.909 -1.903	H 2.788 -4.037 -2.671
H -4.633 2.351 -1.588	H -4.559 2.406 -1.746	H -3.923 2.964 -2.157	H -4.595 2.435 -1.674	H 3.978 -2.810 -2.269
C -0.975 -2.081 2.629	C -1.037 -2.251 2.635	C -1.854 -1.551 2.682	C -1.308 -2.007 2.478	C 1.803 1.445 2.728
H -1.596 -1.206 2.433	H -1.627 -1.348 2.485	H -2.246 -0.650 2.213	H -1.930 -1.188 2.117	H 2.204 0.573 2.211
C -1.049 -2.409 -2.505	C -1.319 -2.280 -2.489	C -1.037 -2.787 -2.224	C -0.535 -2.533 -2.567	C 0.942 2.915 -2.103
H -1.703 -1.540 -2.409	H -1.959 -1.418 -2.292	H -1.454 -1.789 -2.366	H -1.196 -1.666 -2.578	H 1.374 1.930 -2.294
C 4.714 0.056 -0.007	C 4.832 -0.063 -0.217	C 4.828 0.382 0.829	C 4.751 0.174 0.344	C -4.866 -0.247 -0.599
C 2.716 3.057 -0.009	C 2.913 2.927 0.461	C 3.215 0.078 -2.393	C 2.795 3.074 -0.591	C -2.931 -0.793 2.410
H 1.651 3.262 -0.021	H 1.857 3.113 0.615	H 2.178 0.051 -2.703	H 1.735 3.234 -0.751	H -1.867 -0.832 2.609
C -3.855 0.162 -0.471	C -3.831 0.257 -0.457	C -3.600 0.641 -1.050	C -3.735 0.083 -0.898	C 3.602 -0.519 -1.094
H -4.776 0.503 -0.004	H -4.762 0.675 -0.076	H -4.549 1.132 -0.840	H -4.759 0.311 -0.602	H 4.566 -0.991 -0.909
H -4.031 0.142 -1.551	H -3.959 0.117 -1.536	H -3.497 0.589 -2.139	H -3.682 0.200 -1.985	H 3.487 -0.436 -2.180

C 5.487 2.542 0.030	C 5.660 2.401 0.019	C 5.911 0.168 -1.533	C 5.555 2.607 -0.166	C -5.701 -0.693 1.834
H 6.555 2.349 0.045	H 6.717 2.225 -0.150	H 6.951 0.203 -1.228	H 6.617 2.450 -0.011	H -6.766 -0.662 1.635
C -1.661 -2.924 3.702	C -1.765 -3.153 3.630	C -2.875 -2.065 3.694	C -2.130 -2.869 3.434	C 2.823 1.920 3.759
H -2.610 -3.343 3.364	H -2.709 -3.529 3.232	H -3.809 -2.366 3.219	H -2.967 -3.357 2.934	H 3.751 2.256 3.294
H -1.856 -2.316 4.589	H -1.978 -2.607 4.553	H -3.103 -1.287 4.427	H -2.531 -2.254 4.245	H 3.066 1.108 4.451
H -1.027 -3.757 4.016	H -1.156 -4.020 3.898	H -2.490 -2.927 4.245	H -1.517 -3.649 3.892	H 2.432 2.748 4.355
C 4.260 -2.677 -0.034	C 4.212 -2.761 -0.528	C 3.957 0.659 3.453	C 4.186 -2.486 0.921	C -4.277 0.190 -3.279
H 4.099 -3.750 -0.043	H 3.998 -3.815 -0.657	H 3.641 0.769 4.483	H 3.988 -3.526 1.147	H -4.072 0.359 -4.329
C -0.103 -4.178 -1.024	C -0.290 -4.124 -1.159	C -0.747 -4.392 -0.340	C 0.285 -4.173 -0.875	C 0.635 4.418 -0.139
H 0.198 -4.688 -1.932	H -0.052 -4.596 -2.106	H -0.409 -5.109 -1.081	H 0.741 -4.707 -1.701	H 0.278 5.164 -0.842
C 5.012 3.840 0.036	C 5.196 3.699 0.262	C 5.580 0.048 -2.889	C 5.077 3.869 -0.534	C -5.234 -0.937 3.130
H 5.707 4.672 0.057	H 5.902 4.521 0.277	H 6.373 -0.011 -3.624	H 5.779 4.686 -0.660	H -5.948 -1.091 3.931
C -1.717 -3.404 -3.453	C -2.059 -3.231 -3.428	C -1.769 -3.769 -3.137	C -1.071 -3.582 -3.540	C 1.647 3.949 -2.978
H -2.637 -3.820 -3.038	H -2.941 -3.672 -2.958	H -2.823 -3.868 -2.876	H -2.043 -3.971 -3.234	H 2.704 4.051 -2.726
H -1.051 -4.240 -3.683	H -1.417 -4.053 -3.755	H -1.320 -4.765 -3.088	H -0.385 -4.430 -3.624	H 1.186 4.935 -2.875
H -1.959 -2.916 -4.400	H -2.381 -2.697 -4.325	H -1.707 -3.437 -4.177	H -1.176 -3.151 -4.539	H 1.575 3.666 -4.032
C -4.016 2.765 1.088	C -3.964 2.995 0.891	C -3.782 3.203 0.600	C -4.390 2.333 1.081	C 3.868 -3.126 0.479
H -4.931 2.170 1.019	H -4.893 2.420 0.841	H -4.726 2.726 0.323	H -5.226 1.711 0.747	H 4.796 -2.618 0.204
H -4.086 3.321 2.029	H -4.038 3.618 1.790	H -3.972 3.731 1.543	H -4.648 2.677 2.090	H 4.081 -3.673 1.405
C -4.023 -1.544 1.396	C -4.058 -1.168 1.618	C -4.483 -0.917 0.747	C -4.142 -1.860 0.688	C 4.453 1.008 0.748
H -3.684 -2.521 1.741	H -3.850 -2.140 2.065	H -4.412 -1.925 1.162	H -3.816 -2.867 0.958	H 4.352 2.000 1.193
H -5.114 -1.566 1.362	H -5.142 -1.027 1.619	H -5.526 -0.750 0.466	H -5.210 -1.909 0.461	H 5.500 0.881 0.458
H -3.724 -0.791 2.126	H -3.617 -0.395 2.248	H -4.228 -0.201 1.527	H -4.012 -1.210 1.552	H 4.222 0.262 1.507
C -3.922 3.742 -0.084	C -3.824 3.884 -0.344	C -3.356 4.204 -0.473	C -4.219 3.536 0.154	C 3.455 -4.110 -0.616
H -4.839 4.339 -0.135	H -4.718 4.509 -0.450	H -4.168 4.917 -0.656	H -5.165 4.084 0.082	H 4.282 -4.797 -0.825
C 5.568 -2.180 -0.009	C 5.526 -2.310 -0.639	C 5.315 0.630 3.151	C 5.492 -2.009 0.952	C -5.595 0.116 -2.840
H 6.403 -2.871 0.000	H 6.317 -3.020 -0.850	H 6.040 0.718 3.951	H 6.299 -2.687 1.206	H -6.401 0.231 -3.556
C -4.019 -2.311 -0.948	C -4.185 -2.238 -0.599	C -4.118 -1.771 -1.525	C -3.727 -2.306 -1.689	C 4.051 1.918 -1.496
H -3.720 -2.125 -1.978	H -3.924 -2.203 -1.655	H -3.579 -1.690 -2.468	H -3.272 -1.988 -2.627	H 3.504 1.854 -2.437
H -5.111 -2.303 -0.910	H -5.272 -2.156 -0.518	H -5.172 -1.562 -1.723	H -4.811 -2.321 -1.831	H 5.109 1.744 -1.710
H -3.682 -3.308 -0.656	H -3.894 -3.212 -0.200	H -4.046 -2.799 -1.163	H -3.408 -3.327 -1.469	H 3.955 2.932 -1.100

Table S6 Energies for the first 20 excited states for CMA1 in the S_1^P and T_1^P geometries from TD-DFT calculations. *E* is state energy. Calculated oscillator strengths (osc) are for vertical excitations from the S_1^P / T_1^P to the S_n / T_n wave functions in the appropriate geometry, normalized to the strength of the $S_0 \rightarrow S_1$ vertical transition in the coplanar geometry. PIA indicates the expected position of the associated photoinduced absorption.

	S_1^P geometry				T_1^P geometry			
State	$E(S_n)$ **(eV)**	$\Delta E(S_n\text{-}S_1)$ **(eV)**	**PIA (nm)**	**osc/S_1^P**	$E(T_n)$ **(eV)**	$\Delta E(T_n\text{-}T_1)$ **(eV)**	**PIA (nm)**	**osc/S_1^P**
S_1/T_1	2.44				2.43			
S_2/T_2	3.05	0.61	2032	0.001	3.06	0.63	1968	0.012
S_3/T_3	3.83	1.39	892	0.003	3.13	0.7	1771	0.034
S_4/T_4	3.87	1.43	867	0.022	3.62	1.19	1042	0.009
S_5/T_5	3.98	1.54	805	0.005	3.85	1.42	873	0.313
S_6/T_6	4.07	1.63	760	0.018	3.91	1.48	837	0.023
S_7/T_7	4.16	1.72	720	0.263	4.02	1.59	779	0.004
S_8/T_8	4.55	2.11	587	0.001	4.17	1.74	712	0.015
S_9/T_9	4.61	2.17	571	0.018	4.24	1.81	685	0.007
S_{10}/T_{10}	4.69	2.25	551	0	4.33	1.9	652	0.047
S_{11}/T_{11}	4.79	2.35	527	0.156	4.54	2.11	587	0.194
S_{12}/T_{12}	4.82	2.38	521	0.05	4.58	2.15	576	0.228
S_{13}/T_{13}	4.89	2.45	506	0.026	4.6	2.17	571	0.379
S_{14}/T_{14}	4.92	2.48	500	0.006	4.78	2.35	527	0.002
S_{15}/T_{15}	4.94	2.5	496	0.294	4.83	2.4	516	0.212
S_{16}/T_{16}	5.05	2.61	475	0.166	4.87	2.44	508	0.145
S_{17}/T_{17}	5.11	2.67	464	0.012	4.9	2.47	502	0.014
S_{18}/T_{18}	5.34	2.9	427	0.408	4.96	2.53	490	0.05
S_{19}/T_{19}	5.37	2.93	423	0.982	5.03	2.6	476	0.117
S_{20}/T_{20}	5.4	2.96	419	1.418	5.08	2.65	467	0.011

Author Contributions

D.D. and L.Y. developed and characterized the OLED devices. A.S.R. set up the collaboration and performed the molecular design, synthesis, X-ray crystallography and electrochemistry. D.D., L.Y. and S.J. carried out the cryogenic ns-µs transient and steady-state photoluminescence studies. D.D. and L.Y. performed the transient electroluminescence experiments. J.M.R. carried out the ultrafast photoluminescence studies. J.P.H.R. performed the transient absorption measurements. T.H.T. performed the Raman measurements. M.A.J. performed the photothermal deflection measurements. M.B. conceived the initial concept of the emission mechanism. M.L. carried out the quantum chemical calculations. D.C., M.B. and D.D. planned the project and designed the experiments. D.D., D.C., M.B., L.Y. and R.H.F. co-wrote the manuscript.